PHYSICAL REVIEW B VOLUME 47, NUMBER 7 15 FEBRUARY 1993-I

Evolution of the optical functions of thin-film aluminum: A real-time spectroscopic ellipsometry study

Hien V. Nguyen, Ilsin An, and R. W. Collins
Materials Research Laboratory and Department of Physics, The Pennsylvania State University, University Park, Pennsylvania 16802
(Received 13 July 1992; revised manuscript received 14 September 1992)

We report a comprehensive study of the optical functions of thin-film aluminum from initial nucleation through continuous film growth. This study relies on ellipsometric spectra from 1.3 to 4.0 eV collected in real time with a multichannel instrument during both thermal evaporation and magnetron sputtering of Al onto SiO_2 substrates at room temperature. The spectra for all films in the particle growth regime can be modeled with a Maxwell-Garnett-type effective medium theory, modified to include dipole interactions between spheroidal particles arranged on a square grid. The dielectric functions of the Al particles themselves, as well as those of continuous films, are interpreted assuming variable relaxation times for both Drude and interband electronic contributions. The relaxation times are determined by a common value of the mean free path, reduced from its bulk film value owing to electron scattering at defects, particle surfaces, and grain boundaries. For all films in the particle regime of growth, i.e., for thicknesses $< \sim 50$ Å, the deduced relaxation times are independent of thickness (and hence particle size), and are more than an order of magnitude lower than bulk film values. This suggests a defective structure in which electron scattering at internal particle defects limits the relaxation time and determines the particle optical functions. For Al prepared by high-rate evaporation, a transition is observed at a thickness of 55–60 Å, just after continuous film formation. At the transition, the interband electron relaxation time increases abruptly, signaling the development of higher-quality crystalline grains that extend throughout the film thickness. Only after this transition is the (200) parallel-band absorption feature visible in the Al dielectric function at 1.5 eV. For thicknesses > 60 Å, the interband relaxation time increases with thickness, providing evidence that grain-boundary scattering is the dominant mechanism controlling the optical properties in the bulk film stage.

I. INTRODUCTION

The significant differences between the optical properties of ultrathin metal films and those of thick films and bulk materials have been recognized for more than a century. The brilliant colors of ultrathin films, when viewed under white light illumination, were first observed by Faraday, who ascribed the effects to an aggregated, discontinuous morphology of the films.[1] Maxwell-Garnett developed a theoretical explanation of the colors which were caused by "anomalous" optical-absorption bands not present in thick films or bulk materials.[2] This explanation involved treating the film as a slab of composite material having spherical metal particles embedded in the ambient medium. The particles were assumed to exhibit bulk film optical response and to interact in accordance with the Lorentz local field description. It was not until much later that the discontinuous nature of ultrathin metal films was observed directly by electron microscopy.[3]

Several refinements for calculating the effective optical functions of discontinuous metal films have been proposed since the development of the original Maxwell-Garnett effective medium theory (EMT). For example, the simple theory was extended by treating the film as a composite material having identical spheroidal particles with their axes of symmetry normal to the substrate.[4,5] Later, a generalized EMT was developed in which such spheroids were arranged on a surface and the interparticle interaction was calculated as that from a two-dimensional array of dipoles.[6–9] In one case, the fields due to the images of the dipoles in the substrate surface were also included in this calculation.[8]

In an early study of discontinuous Au "particle" films, Doremus used morphological quantification by electron microscopy, along with the bulk dielectric function for the Au particles, in order to calculate the effective film optical functions from the original Maxwell-Garnett EMT.[10] Excellent agreement was obtained between the wavelength of the maximum in the absorption spectra derived from the simple EMT and that obtained experimentally using a normal incidence measurement geometry. The agreement led to the conclusion that it was unnecessary to account for the details of particle shape in order to explain the general features of the effective optical response of the films and that the more complex interparticle interactions applied in the generalized EMT were also unnecessary. The widths of the observed absorption bands were not in agreement with theory, however. This effect was attributed to free-electron scattering at particle surfaces that limits the mean free path and influences the dielectric function of the particle.

In work over a decade later on the same system, a generalized EMT similar to that of Ref. 9 was used in which the particles were represented as a two-dimensional array of spheroids with symmetry axes along the substrate.[11]

 ©1993 The American Physical Society

Electron microscopy was also used to characterize the morphology of the particle film,[12] and the resulting mean eccentricity of the particles, distribution of semiaxes, and average interparticle spacing were all used as input to the EMT. A particle size dependence in the free-electron contribution to the Au dielectric function was included as well. Sufficient agreement was obtained between the results of the EMT calculation and normal incidence transmittance spectra to permit the authors to state confidently that the optical properties of metal particle films are governed entirely by their morphology.

Interest in the optical properties of particle films has waned over the past decade or more, possibly because of this suggestion that predicting the optical properties was simply a matter of careful morphological analysis, and thus the belief that there were no new scientific insights to be gained. In addition, any potential advances in understanding such films in greater detail were limited by the available experimental optical probes. Over the last decade, research on the effects of morphology on the optical properties of metal films has taken two directions. The first has involved explaining the interesting wavelength-independent near-infrared transmittance and reflectance spectra of metal films near the percolation threshold.[13–15] Recently, a scaling theory of the percolation transition has been developed.[16] The second direction has involved developing techniques for morphological characterization of metal films that employ advances in ellipsometric measurements and analysis.[17] Because this latter direction is relevant for the present investigation, it deserves additional comment here.

With the development of multilayer optical computation embedded within a least-squares regression analysis program, photon-energy-independent parameters that characterize the morphology of continuous films can be deduced from spectroscopic ellipsometry (SE) data.[18] The analysis technique typically includes the Bruggeman EMT to model density-deficient surface and subsurface layers,[19] although other theories that appear specific to certain morphologies have also been applied more recently.[20,21] The importance of this work is that it has provided insights into the origin of the substantial differences between the optical properties of supposed bulklike continuous metal films prepared and measured in different laboratories. These differences were found to arise, not from the measurement technique, but from sample-to-sample variations.[17] As a result, comparative estimates of bulk film (subsurface) void volume fraction as well as surface roughness thickness can now be made from an analysis of the spectral variation in the ellipsometric parameters (ψ,Δ). The capability of a nondestructive optical technique such as ellipsometry to provide detailed information on metal surface and bulk film quality is important in a wide variety of technological applications.

With the present study, optical characterization is extended further, and we report real-time spectroscopic ellipsometry determination of the optical functions of metal films, from measurements performed continuously throughout the stages of nucleation, coalescence, and bulk film growth. We build on the experiences of others in efforts to deduce information on the evolution of the morphological and electronic properties for the aluminum thin-film system, solely from the real-time SE measurements. This is an important goal because the optical approach, in contrast to direct probes of morphology, is nondestructive, noninvasive, and requires no specialized equipment internal to the deposition system. We seek to establish the minimum theoretical input needed to understand the evolving optical data, applying the least-squares regression analysis described in the previous paragraph. Because of the capability of determining both real and imaginary parts of the dielectric function of aluminum films, using approaches previously demonstrated for static films, it becomes easier to extract the role of morphology in order to deduce information on the electronic behavior.

In this paper, primary emphasis will be placed on the interpretation of the evolution of electronic behavior for the aluminum thin-film system, which shows surprisingly clear trends in the different stages of growth. Because a simplified morphological model that neglects statistical distributions in the size and shape of aluminum particles or grains is used, we are somewhat less confident of the deduced morphological information; as a result, less emphasis will be placed on its interpretation. We expend considerable effort, however, demonstrating that the simplified morphological model does not compromise the integrity of the information on the electronic behavior.

Aluminum has been chosen for this study of the evolution of metal film optical properties for three reasons, the obvious one being technological. More importantly from the standpoint of the interpretation of our results, however, the bulk film optical functions of Al can be expressed as a function of photon-energy-independent parameters using the description of Ashcroft and Sturm.[22] In contrast, the optical functions of the noble metals, widely used in earlier *ex situ* morphological and optical studies of metal particle films, are not amenable to such interpretation. The description for Al includes the free-electron or Drude contribution, as well as interband contributions from two sets of transitions that dominate all others as a result of the "parallel-band" effect.[23] In Al this effect occurs in the neighborhood of Brillouin-zone surfaces parallel to the hexagonal (111) and square (200) zone faces. These parallel-band transitions produce sharp onsets in absorption at $2|U_{111}|=0.49$ eV and $2|U_{200}|=1.53$ eV (values deduced from an analysis of de Haas–van Alphen measurements[24]) that gradually fall off at higher energies. Here U_K is the Fourier coefficient of the pseudopotential for the reciprocal lattice vector K that corresponds to the appropriate zone face. Thus, the third reason for the choice of Al is that the (200) parallel-band transition and, in particular, its strong high-energy tail span the most sensitive spectral region of our ellipsometer detection system. Thus, information on the electronic behavior can come not only from the Drude contribution, but also from the parallel-band contribution, whose analytical form is described in Ref. 22.

The disadvantages of the choice of Al for this study include its low atomic number, small particle size in the nucleation stage (<50 Å), and higher reactivity in comparison to the noble metals. As a result, reliable comparison

of the morphology of Al particle films deduced *in situ* by optical methods with that deduced *ex situ* by direct electron microscopy is difficult. For example, postoxidation can consume the particles over time, and this alone, or in combination with etching procedures used for sample processing, is expected to alter the particle size and/or shape observed *ex situ* from that measured in real time. Thus, such a comparison is beyond the scope of the present investigation, and must await further efforts. Where appropriate, we refer to earlier direct studies of morphology that employ Al film preparation methods and substrates similar to the present one.

This paper elaborates on and extends a previous report[25] and is organized as follows: In Sec. II we describe methods of sample preparation along with studies undertaken to ensure that substrate-film chemical interactions are negligible. Such effects would excessively complicate interpretation of the optical data. Section II also includes an abbreviated description of the data collection methods of real-time SE. Section III A presents an analysis of the dielectric function of Al obtained in real time in the bulk stage of film growth, in comparison both with earlier experimental studies of static films and with the Ashcroft-Sturm analytical form. Then an overview of the dielectric functions in the various stages of film growth is presented. In this case we focus on a film prepared at high rate, which leads to a high nucleation density, an abrupt transition from the particle regime to the continuous film regime, and a thick film density believed to be near the single-crystal value. In Sec. III A we stress the inability of a simple morphological model with bulk film optical functions to describe the ellipsometric data in the early growth stages. In Sec. III B the continuous film growth regime is discussed in detail. In this regime, we observe the development of the (200) parallel-band feature as a function of film thickness, which provides evidence of a crystallization phenomenon and then continuous information on grain size as a function of thickness. In Sec. III C the particle film growth regime is discussed in detail. The focus here is on the development of an appropriate effective medium theory which enables us to exact the morphology so that reliable information on the electronic characteristics of the particles themselves can be deduced. In Sec. IV our results will be discussed in view of earlier optical studies of static metal films and particles that are found to be relevant.

II. EXPERIMENTAL DETAILS

For the most part, our study focuses on Al films prepared by evaporation from a tungsten coil onto thermally oxidized silicon wafers at 25 °C. Real-time results will be presented for two thin films deposited at physical thickness rates of 280 and 43 Å/min, time-averaged over the full deposition. The ratio of the vacuum pressure to the deposition rate is a measure of the arrival rate of vacuum residual gas atoms relative to that of Al atoms. For the evaporation of both films, these ratios were $\sim 10^{-9}$ Torr min/Å, ensuring negligible contamination at least for the purposes of optical property measurements.[26] For the high- and low-rate films, the substrate oxide thicknesses were 71 and 110 Å, respectively. These values were determined from ellipsometric spectra collected at time zero prior to Al deposition, using least-squares regression analysis and literature optical functions of Si (Ref. 27) and vitreous SiO_2 (Ref. 28) measured at room temperature.

The lower evaporation rate led to a lower nucleation density, as would be expected based on homogeneous nucleation theory whereby the capture radius for each nucleus expands as the time available for surface diffusion increases.[29] The lower nucleation density ensured a wider thickness range over which Al particle growth could be monitored. After coalescence of initial Al nuclei, the high-rate film exhibited optimum morphological uniformity including a high bulk film density, assessed by ellipsometry as described below. Thus, we concentrate on the low-rate film to study the particle growth regime, and the high-rate film to study the regime of particle contact and subsequent bulk film growth.

Real-time SE results are also presented in the particle growth regime for an Al film prepared by dc magnetron sputtering, for comparison with the corresponding results obtained by low-rate evaporation. In this case, the substrate was a Si wafer with an 88-Å thermal oxide, the base pressure was $\sim 5\times 10^{-8}$ Torr, the operating Ar pressure was 5×10^{-3} Torr, and the dc power was 100 W for a target 2.5 cm in diameter. Under these conditions, the average deposition rate was 36 Å/min, similar to that of the low-rate-evaporated film.

In order to assess the possibility that the Al films react with SiO_2 substrates to form Al_2O_3 and an underlying layer of Si (Ref. 30), representative Al depositions were performed on SiO_2 using both evaporation and sputtering techniques. After preparation and removal from the deposition chamber, these films were dissolved in 5-vol% HCl in H_2O, and the exposed substrate surfaces were studied by *ex situ* SE using a rotating analyzer ellipsometer with high precision and accuracy. We found that in all cases the ellipsometric spectra for the substrate, and in particular the oxide thicknesses, remained unchanged from those measured prior to film growth, at least to within the confidence limits of ± 1 Å. This indicates the absence of a SiO_2/Al chemical interaction at room temperature beyond the level of a single monolayer.

Figure 1 shows a schematic of the instrument used for real-time SE studies. It consists of the following components: Xe arc source, collimator, rotating polarizer, sample in vacuum chamber, fixed analyzer, spectrograph, 1024-element Si photodiode array, and associated detector controller.[31] For all real-time SE measurements, the angle of incidence was 70°, and the analyzer was oriented at 30° with respect to the plane of incidence. In this rotating polarizer configuration and in the absence of errors, the irradiance wave form at any given element of the detector array exhibits only nonzero dc and 2ω Fourier components. Here $\omega/2\pi$ is the polarizer rotation frequency, 12.5 Hz in our case. The array is read every $\pi/4$ radians of polarizer rotation, triggered by an optical encoder mounted on the polarizer motor shaft. The integrated photon-count levels from four consecutive readouts provide the dc-normalized $\cos 2\omega t$ and $\sin 2\omega t$

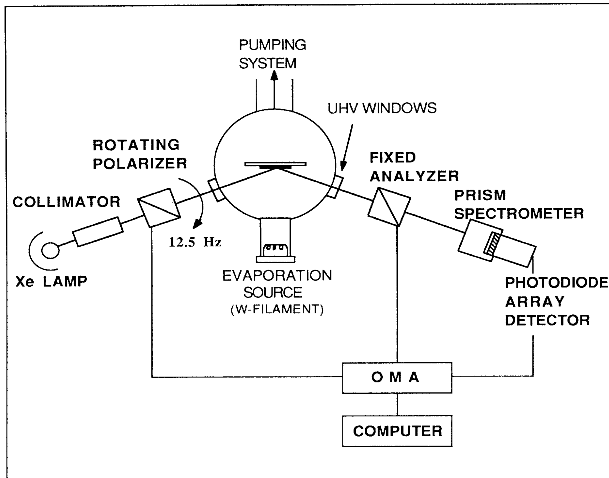

FIG. 1. Schematic of the rotating polarizer, multichannel ellipsometer applied in real-time SE studies of Al thin films prepared by sputtering and evaporation. The system configuration for evaporation is shown here. [OMA denotes optical multichannel analyzer (Ref. 36)].

coefficients (α and β), along with a consistency relationship.[31–33] From (α,β) values for all detector elements, spectra in the ellipsometry angles (ψ,Δ) can be computed after calibrations are performed that determine (1) the angle of the polarizer transmission axis with respect to the plane of incidence at $t=0$ (defined by an electronic trigger) and (2) the center photon energy for each detector element.[33] As usual, ψ and Δ are defined by

$$\tan\psi\exp(i\Delta)=r_p/r_s,$$

where r_p and r_s are the complex amplitude reflection coefficients for p- and s-polarization states.[34] Additional details of the ellipsometer including polarizer calibration and correction procedures for source, polarization system, and detector errors can be found elsewhere.[33,35]

The detector element grouping capability of the detector controller[36] is employed in order to collect 83 spectral positions over the useful photon-energy range from 1.3 to 4.0 eV. With a polarizer rotation period of 80 ms, a single pair of (ψ,Δ) spectra can be collected in an optical cycle of 40 ms. Depending on the deposition rate, however, time resolution can be sacrificed for signal-to-noise ratio by averaging spectra over an even number of consecutive optical cycles—typically, 8–20 for these depositions. For the high and low rate evaporated films and the sputtered film, the repetition times for such spectra were 1.25, 5.5, and 1.5 s, respectively.

III. RESULTS

A. The optical functions of Al films throughout nucleation and growth stages

We will first provide an overview of the optical functions of Al deduced from ellipsometric spectra in different stages of the deposition process from nucleation to bulk film growth. This analysis is best performed on the high-rate Al evaporation, as this film exhibits final optical functions closest to those in the literature for smooth, high-density films.

Figure 2 (top) shows the imaginary part of the pseudodielectric function $\langle\epsilon_2\rangle$ collected in real time during the deposition of high rate Al. The pseudodielectric function $\langle\epsilon\rangle=\langle\epsilon_1\rangle+i\langle\epsilon_2\rangle$ is defined such that a single ideal interface between the ambient vacuum and a hypothetical material of dielectric function $\langle\epsilon\rangle$ gives the same (ψ,Δ) values as the $Al/SiO_2/Si$ multilayered structure. Thus, from the Fresnel equations,[34]

$$\langle\epsilon\rangle=\sin^2\theta\{1+[(1-\rho)/(1+\rho)]^2\tan^2\theta\}, \quad (1)$$

where θ is the angle of incidence. The three-dimensional surface in Fig. 2 at the top was constructed from 121 spectra, each having 83 photon-energy positions from 1.3 to 4.0 eV. At the front of the plot, the pseudodielectric function of the bare SiO_2/Si substrate is visible with the sharp feature at 3.35 eV arising from the E_0'-E_1 transi-

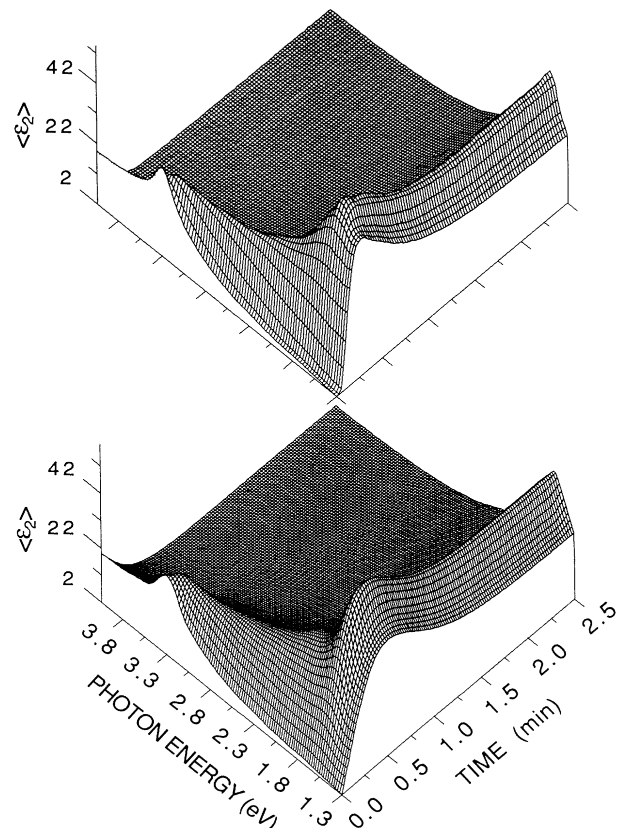

FIG. 2. Imaginary part of the pseudodielectric function collected in real time during high-rate (280-Å/min) Al evaporation onto a room-temperature Si wafer covered with a 71-Å thermally grown SiO_2 layer (top). A total of 121 spectra, each consisting of 83 data points, were collected over a deposition time of 150 s. Calculated results appear at the bottom for a theoretical optical model in which Al grows perfectly uniformly on the SiO_2/Si substrate assuming a thickness-independent dielectric function.

tions of the underlying Si (Ref. 27). As deposition proceeds, the Si feature is rapidly damped, and the (200) parallel-band feature near 1.5 eV for the Al film builds up and dominates the spectrum after about 1 min. At the back of the plot, the Al is virtually opaque to the incident photon energies with an estimated thickness of 700 Å. At this point, $\langle \epsilon_2 \rangle$ differs from the true imaginary part of the dielectric function ϵ_2 for the Al film, only owing to the possible presence of a surface roughness layer or heterogeneities through the optical penetration depth.

For comparison, the lower part of Fig. 2 shows the corresponding set of spectra expected for the uniform growth of Al onto the SiO_2/Si substrate calculated assuming a thickness-independent Al dielectric function, obtained from the final experimental $\langle \epsilon_2 \rangle$ spectrum of the upper part of the figure. Although the same overall trends are observed in the experimental data and the calculated result, one interesting difference can be detected in the initial stages. A careful look at the grid lines on both surfaces near 1.5 eV reveals that the (200) parallel-band feature in the experimental data builds up more slowly than that in the calculation. In the demonstrated absence of a substrate reaction, this effect is attributable to a thickness dependence in the Al optical properties. In Secs. III B and III C, the underlying physical origin of this observation will be discovered.

Our first step in the analysis of the deposition of Fig. 2 is to assess the optical properties of the final film ($\sim$700 Å, after 150 s), in comparison with the best available data in the literature. For the latter, we use the dielectric function of Shiles *et al.*,[37,38] obtained from reflectance measurements of films prepared and maintained in ultrahigh vacuum. Over the photon-energy range of 0.7 to 2.5 eV, these results closely match those of Mathewson and Myers[39] obtained from *in situ* SE measurements of similarly prepared films. Thus, we applied least-squares regression analysis to the final $(\langle \epsilon_1 \rangle, \langle \epsilon_2 \rangle)$ spectra for our opaque Al using a three-medium (ambient-roughness-bulk) model, the Bruggeman effective medium approximation,[17,19] and the ϵ data of Ref. 38. The following photon-energy-independent morphological information was deduced: relative void volume fractions of 0.001 ± 0.005 for the bulklike layer and 0.51 ± 0.02 for the surface roughness layer, and a roughness-layer thickness of 10.5 ± 0.5 Å. Because our final film has a void fraction in the bulk layer identical to that of Shiles *et al.*,[37,38] both films most likely exhibit single-crystalline density.

Next, the 10-Å roughness layer was analytically removed from the final $(\langle \epsilon_1 \rangle, \langle \epsilon_2 \rangle)$ to reveal the true dielectric function of the bulk layer for the high-rate Al film, designated ϵ_b. The result appears in Fig. 3 for comparison with the data of Ref. 38. The primary difference between the two dielectric functions is the sharper parallel-band feature for our film, suggesting a larger final grain size (see Sec. III B).

We then proceeded to fit ϵ_b to the Ashcroft-Sturm formula, expressed as

$$\epsilon_{AS}(\omega) = 1 + (4\pi i \sigma_a/\omega) \left\{ 32 a_0 k_F (E_F \tau_D / h) / [(m_{opt}/m_e)(1 - i\omega\tau_D)] + \sum_K (a_0 K) J_K(\omega, |U_K|, \tau_K) \right\}, \quad (2)$$

where a_0 is the Bohr radius; $\sigma_a = (e^2/12 a_0 h)$; k_F and E_F are the Fermi wave vector and energy; τ_D is the Drude electron relaxation time; and m_{opt}/m_e is the Drude optical mass relative to the electron mass.[22] Thus, we include the Drude contribution (first two terms) and the parallel-band contributions (third summation) to the dielectric function; however, normal-band contributions are neglected. For the parallel-band summation, U_K and τ_K are the Fourier coefficient of the pseudopotential and the phenomenological relaxation time, respectively, associated with the transitions for wave vector K. The J_K are complex-valued functions presented in Ref. 22. In the summation of Eq. (2), we include the two terms due to the transitions associated with the (200) and (111) families of Brillouin-zone faces.

The Drude contribution to the imaginary part of the bulk film dielectric function ϵ_b of Fig. 3 is small compared to the (200) parallel-band contribution. In addition, τ_D is long enough so that $\omega\tau_D \gg 1$ over our spectral range, and the real part of ϵ_b is also nearly independent of τ_D. Thus, in fitting ϵ_b to Eq. (2) by least-squares regression analysis, τ_D was fixed at its bulk film value from the literature: $\tau_{D,b} = 10.6 \times 10^{-15}$ s (Ref. 38). In addition, the (111) parallel-band contribution to ϵ_b is weak above 1.3 eV. As a result, we used the literature value $|U_{111}| = 0.25$ eV and set

$$\tau_{111,b} = \tau_{200,b} \equiv \tau_{PB,b} .$$

We also set m_{opt}/m_e equal to the theoretical bulk value of 1.55 (Ref. 22). With these constraints, a fit to ϵ_b in the neighborhood of the (200) parallel-band transition provided

$$|U_{200}| = 0.73 \text{ eV},$$
$$\tau_{PB,b} = 4.1 \times 10^{-15} \text{ s}.$$

These values are in excellent agreement with the room-temperature results of Mathewson and Myers,[39] who found

$$|U_{200}| = 0.74 \text{ eV},$$
$$\tau_{PB,b} = 3.8 \times 10^{-15} \text{ s}.$$

If $|U_{200}|$ and $\tau_{PB,b}$ are fixed at our best-fit values, then the value of m_{opt}/m_e that provides the best fit over the full spectral range is 1.62. This is to be compared with the experimental result of 1.60 obtained by Shiles *et al.*[38] It now should be clear that the real-time SE capability together with the Ashcroft-Sturm formula provide an opportunity to characterize the evolution of the electronic properties as a function of film thickness. These efforts will be undertaken in Secs. III B and III C.

Next it is instructive to present a first attempt at understanding the evolution of the optical spectra of the high-rate Al film (as shown in Fig. 2) solely in terms of morphological development. Here we again utilize the least-squares regression analysis techniques of morphological characterization developed by Aspnes,[18] and applied successfully to static Au (Ref. 17) and amorphous silicon (*a*-Si) (Ref. 40) films. In this analysis, optical functions of density-deficient layers are calculated from the bulk film optical functions and the void volume fractions of the layers using the Bruggeman EMT. The bulk optical functions of the Al are calculated analytically from the Ashcroft-Sturm formula using the combination of fixed and best-fit parameters of the previous paragraph. In order to select the appropriate optical model (e.g., one or two layers for the Al film), we use the criteria developed in a recent real-time SE study of *a*-Si films.[41]

Figure 4 shows the outcome of the analysis for the high-rate Al film. In the first 6 s, we employ a one-layer model for the film with two free parameters, the void volume fraction in the layer and the layer thickness. Over this time scale, the void fraction drops from unity (no film) to zero as the film thickness increases to about 50 Å, as would be expected for isolated nuclei that increase in size and make contact. The unbiased estimator of the mean-square deviation, σ, a measure of the quality of the regression analysis fit[18] is plotted at the bottom in Fig. 4. σ increases significantly in the first 6 s of deposition, indicating a serious problem with our optical model in the nucleation stage.

For $t \geq 7.5$ s in Fig. 4, a two-layer (roughness-bulk) model for the Al film is employed. This time range is considered in two separate segments. First, for 7.5 s $\leq t \leq 30$ s, the Al film is semitransparent and the bulk film thickness can be determined with reasonable confidence. In this segment, the void volume fractions for the surface and underlying layers are fixed at 0.5 and the bulk film value, respectively, in order to avoid problems associated with the correlation of variables. The total film thickness increases linearly with time here, whereas the surface roughness layer decreases somewhat from 7–8 Å to $\sim$3 Å. Second, for $t \geq 60$ s, the film is opaque and no accuracy is lost by omitting the substrate

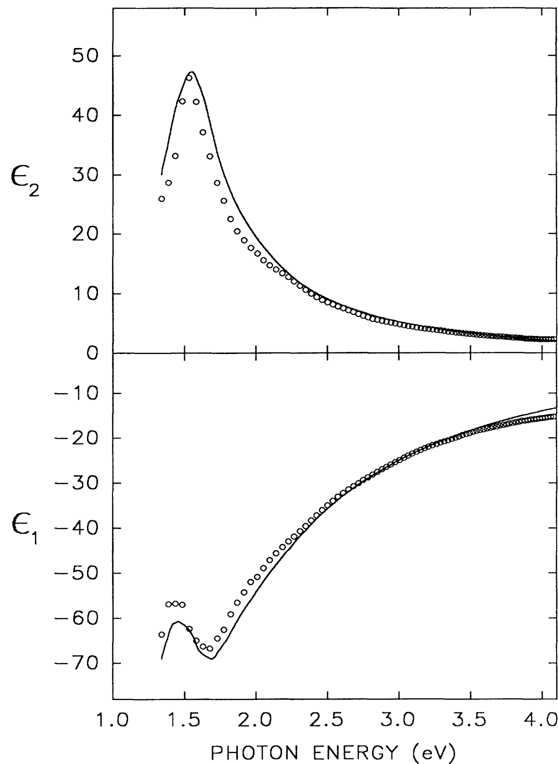

FIG. 3. Dielectric function of bulk film Al, measured in real time during growth by high-rate (280-Å/min) evaporation onto room-temperature SiO_2/Si (open circles). These results were deduced from the final (150-s) pseudodielectric function of the deposition of Fig. 2, after correcting for a 10-Å surface roughness layer. The solid line is the dielectric function reproduced from Ref. 38 for comparison.

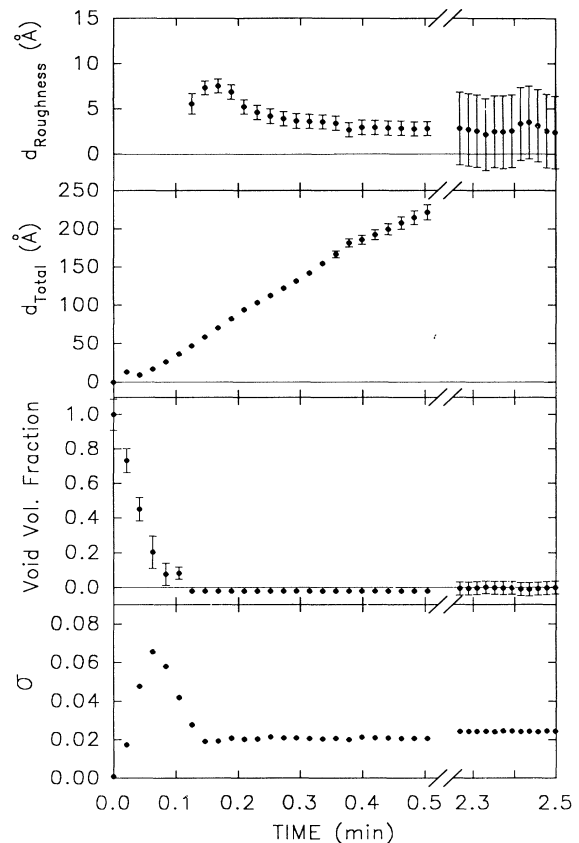

FIG. 4. Interpretation of the evolution of optical properties for the high-rate-evaporated Al film using a morphological model. Least-squares regression analysis was used to deduce the photon-energy-independent parameters of surface roughness thickness, total film thickness (roughness plus bulk layer), and bulk-layer void volume fraction (from top to bottom). The bottom panel shows σ, the unbiased estimator of the mean-square deviation for the fit. In this analysis, we applied the dielectric function generated analytically from Eq. (2) with fixed bulk film values for parametrization. In the first 6 s, a one-layer model is used for the Al film; for longer times, a two-layer model is used. Error bars represent the 90% confidence limits.

from the optical model. In this segment, the bulk-layer void fraction is allowed to vary, and a constant value of ~ -0.02 is obtained. In addition, the surface roughness-layer thickness has stabilized at ~ 3 Å, but the confidence limits suggest that it is not required in the optical model. The difference in the deduced morphological parameters between the final film in this analysis (3 Å, -0.02) and that obtained earlier (10.5 Å, 0.00) by comparison to the dielectric function of Shiles *et al.* may arise from minor inadequacies in the Ashcroft-Sturm analytical formula for ϵ_b, whose origins are unknown at this point. Overall, a larger best-fit σ value ($\sim 0.02-0.025$) is obtained using the analytical formula in comparison to that (0.012) using the measured dielectric function of Shiles *et al.*, and this is reflected in the significantly larger confidence limits in Fig. 4 (see far right).

Irrespective of these uncertainties, the main point to be made from Fig. 4 is the exceptionally large σ values in the early nucleation stages. This behavior is common to all Al films prepared by evaporation and sputtering, and the fits cannot be improved significantly by using other simple classical effective medium theories within the same general approach.[40] As a result, we conclude that the experimental data cannot be understood by assuming the bulk film optical functions within a morphological model. Even in the later stages of film growth, we find that this general approach cannot account for the evolution of the (ψ,Δ) spectra for the high rate Al film in the vicinity of the (200) parallel-band feature (see Sec. III B).

In order to uncover the source of such problems, we extract the optical functions directly at different stages in the growth process using the spectroscopic analysis procedure developed for static films by Arwin and Aspnes.[42] The essence of the procedure is to apply a one-layer, isotropic model for the film and choose a trial value for the film thickness, *d*. With this trial value, the experimental (ψ,Δ) [or $(\langle\epsilon_1\rangle,\langle\epsilon_2\rangle)$] spectra can be inverted to obtain a trial dielectric function (ϵ_1,ϵ_2) for the Al film. The latter is inspected in the region near 3.3 eV where the Si substrate exhibits its E_0'-E_1 critical-point structure. If the initial choice of *d* is incorrect, the substrate structure will appear as artifacts in the Al film (ϵ_1,ϵ_2) spectra. The correct value of *d* can be identified based on the minimization of the artifacts.

Figure 5 shows a particularly clear example of the trial dielectric functions for the low-rate Al film (to be discussed in Sec. III C) at $t=36$ s calculated from different thickness choices and smoothed for clarity. Obviously, a 26 ± 0.5-Å-thickness choice minimizes the artifacts and leads to the correct dielectric function. The fact that the artifacts could be eliminated suggests that the one-layer model is close to reality. The validity of the assumption of isotropy will be addressed in Sec. III C.

Figure 6 shows selected dielectric functions determined in this manner from (ψ,Δ) spectra collected during high-rate Al film growth. The ϵ_2 spectrum for the 23-Å film (open circles) features a broad resonance absorption band with a peak energy near 3.4 eV, due to dipolar plasmon-polariton excitations,[43] and ϵ_1 exhibits the associated dispersive behavior. These results are consistent with isolated (but interacting) Al particles. With continued growth, the absorption band increases in magnitude and shifts to lower energies, as indicated by the spectra at 44 Å (solid circles). This effect is observed most clearly for the low-rate-evaporated and -sputtered Al films (see Fig. 10) and, as will be seen in Sec. III C, can be attributed to an increase in the strength of the dipole interaction among the particles.

Returning to Fig. 6, the particles appear to make contact between 44 and 53 Å, and the percolation threshold is evidenced by an abrupt decrease in ϵ_1 from positive to negative values at the lowest photon energies. The thickness value at the percolation threshold ($\sim 45-50$ Å) lies midway within the range of the values reported earlier for evaporated Al films, 20–70 Å.[13,44] For clarity, only ϵ_1 for the 53-Å film is presented in Fig. 6 (solid triangles; ϵ_2 appears in Fig. 18, below). Although metallic optical behavior has developed for the 53-Å-thick film, there is no evidence of the (200) parallel-band feature in ϵ_2 at 1.5 eV (see Fig. 18). This feature develops rather abruptly for film thicknesses between 53 and 61 Å, and dominates the low-energy part of the spectrum for the 106-Å film in Fig. 6. In Sec. III B, we will describe an analysis of the (ψ,Δ) spectra obtained in the continuous growth regime

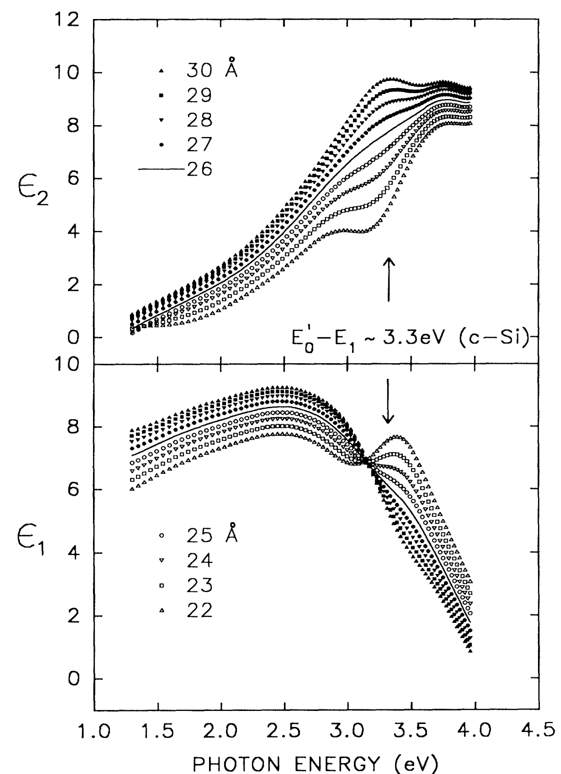

FIG. 5. Trial dielectric functions for Al determined in a one-layer, isotropic analysis of real-time ellipsometric data collected at $t=36$ s during evaporation of Al onto a SiO_2/Si substrate at low rate (43 Å/min). The different choices of the film thickness were made to allow mathematical inversion of (ψ,Δ) [or $(\langle\epsilon_1\rangle,\langle\epsilon_2\rangle)$] and obtain these results. The correct thickness (26 Å) is the one that minimizes artifacts in the inverted dielectric function arising from structure in the substrate optical response.

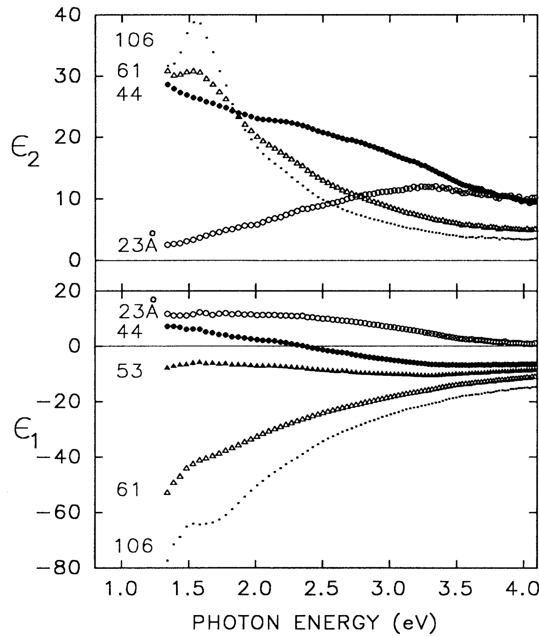

FIG. 6. Selected dielectric functions obtained from real-time spectroscopic ellipsometry observations during high-rate Al growth, applying the one-layer, isotropic analysis technique of Fig. 5. The imaginary part of the dielectric function for the 53-Å-thick film is omitted for clarity (see Fig. 18).

for the high rate Al film ($d > 50$ Å). In this regime, changes in the visibility of the (200) parallel-band feature for $d > 60$ Å in Fig. 6 cannot be attributed to the changes in morphology as modeled in Fig. 4. In fact, as we shall see next, they are associated with changes in the intrinsic Al optical functions as a result of increases in parallel-band electron relaxation time with thickness.

B. Interpretation of the optical functions in the continuous film growth regime

In interpreting the ellipsometric data in the continuous film growth regime, we apply least-squares regression analysis to extract the photon-energy-independent values of film thickness, void fraction, and electron mean free path from (ψ,Δ) data collected during high rate Al film growth. In this analysis, the dielectric function was parametrized according to Eq. (2), and the (200) and (111) parallel-band relaxation times were equated as in the earlier analysis of ϵ_b in Sec. III A. We apply a classical model that assumes a reduction in the electron mean free path λ from its bulk film value.[45] Specifically, the relaxation times τ_j ($j = \mathrm{PB}, D$) in Eq. (2) were related to a single variable value of λ, and the known bulk values $\tau_{j,b}$ according to the relationship

$$\tau_j^{-1} = \tau_{j,b}^{-1} + (v_F/\lambda), \quad (3)$$

where v_F is the Fermi velocity, 2.02×10^8 cm/s.

Although Eq. (3) is strictly valid only for spherical scattering geometry, for simplicity we will use this equation to *define* λ in both particle and continuous film growth regimes. In general, the value of λ in Eq. (3) may be different for the (200) parallel-band and Drude transitions. In the continuous film regime, however, we emphasize the former by obtaining the best fit in the spectral region of the parallel-band feature in ϵ_2. Other parameters needed in Eq. (2) in order to perform regression analysis are fixed at the bulk film values given in Sec. III A. In particular, we fix the optical mass m_{opt} and parallel-band transition energies $2|U_K|$ at bulk values in the expectation that size effects which alter the electronic band structure or conduction electron density are negligible in the continuous film regime. Finally, in order to maintain consistency with the morphological analysis of Fig. 4 for the bulk film, we assume a fixed roughness-layer thickness of 3 Å. This particular feature is not critical to the analysis, since the parameter of interest λ (which is a sensitive function of boundary and defect scattering) is determined for the most part by the shape of the (200) parallel-band feature in ϵ_2.

Figure 7 shows a typical fit to the experimental ϵ_2 results, in this case for the 106-Å-thick film of Fig. 6. Here, the (ψ,Δ) data and their fits are both processed to extract the surface roughness and underlying bulk-layer thicknesses (0.5 volume fraction void for the former) in order to determine the bulk-layer dielectric function. We note here that in general the total film thicknesses deduced through regression analysis match those extracted independently by the Arwin-Aspnes technique (see Fig. 5) within ±5 Å. The thicknesses in the continuous regime in Figs. 6–9 for $d > 50$ Å are standardized as those from the former technique. Also shown in Fig. 7 is the decomposition of the best-fit ϵ_2 spectrum into its Drude and parallel-band contributions. The dominance of the latter is seen clearly.

The values of λ and τ_{PB}, interrelated through Eq. (3), appear in Fig. 8, plotted as a function of the film thick-

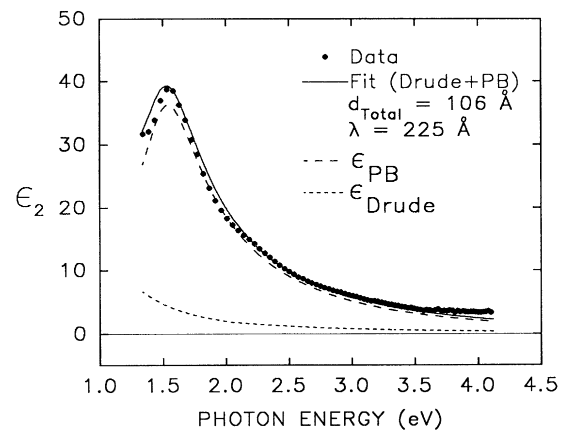

FIG. 7. Imaginary part of the dielectric function for the high-rate Al evaporation of Fig. 6 at a thickness of 106 Å (points). Least-squares regression analysis was used in a fit to these data with void volume fraction, thickness, and electron mean free path as free parameters (solid line). The latter two values are included in the legend. The best-fit dielectric function is decomposed into its Drude and parallel-band contributions (dashed lines).

ness (triangles, for $d > 50$ Å). Other data also appear in Fig. 8 (circles for $d < 60$ Å for the low-rate-evaporated film and triangles for $d < 50$ Å for the high-rate film) which will be discussed in Sec. III C. In Fig. 8, a very interesting effect is observed, namely, the increase in λ by about a factor of 9, from ~ 10 to 90 Å as d increases from 55 to 60 Å. This corresponds to an increase in the parallel-band relaxation time by a factor of 5. This effect is reflected in the relatively rapid appearance of the parallel-band feature between 53 and 61 Å (compare ϵ_2 in Figs. 6 and 18).

We have attempted to fit the dielectric function of the 53-Å-thick film using the single Drude term of Eq. (2), as might be expected for Al in the liquid state.[46] The liquid state could result from a size-dependent reduction in the melting temperature, as has been observed in some other metal particle systems.[47,48] The resulting poor fit implies that it is not possible to ascribe the transition in Fig. 8 to crystal formation from the melt at a thickness of 55–60 Å. It is anticipated, however, that significant atomic diffusion and restructuring can occur upon contact of the particles. Thus, it is more likely that the transition is due to a crystallization phenomenon that occurs when amorphous or nanocrystalline particles make contact and form larger single-crystal grains that extend through the film thickness. Alternatively, the transition may represent the healing of a high density of nucleation-induced defects via a similar process. In any event, prior to the transition, there must be insufficient (200) translational symmetry for observation of a well-defined parallel-band feature. The above alternatives will be discussed further in Sec. IV in view of earlier results from the literature.

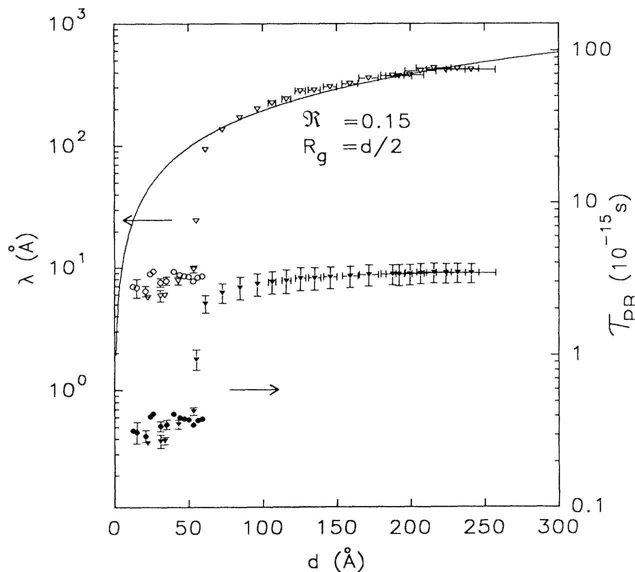

FIG. 8. Electron mean free path (open symbols) and parallel-band relaxation time (solid symbols) as a function of film thickness d determined by least-squares regression analysis of real-time ellipsometry spectra collected during the growth of two Al films (triangles, 280 Å/min; circles, 43 Å/min). The triangles for $d > 50$ Å were determined with a continuous film model and the Bruggeman EMT; all other data were deduced with a particle film model and the generalized Maxwell-Garnett EMT of Eq. (4a). The solid line is fit to λ for $d > 60$ Å using a grain growth model. For a grain radius of $d/2$, the solid line corresponds to a grain-boundary reflection coefficient $\mathcal{R}$ of 0.15. Error bars are representative 90% confidence limits.

Above the transition in Fig. 8, for $d > 60$ Å, both λ and $\tau_{\rm PB}$ increase gradually with d, presumably as a result of a reduction in grain-boundary scattering as the average grain radius R_g increases. To test this hypothesis for the continuous film regime, and to make connection with previous studies,[49] we can make the substitution $\lambda \rightarrow 2[(1-\mathcal{R})/3\mathcal{R}]R_g$ in Eq. (3), where $\mathcal{R}$ is the grain-boundary reflection coefficient.[50] The resulting relationship is appropriate for a spherical geometry and diffuse boundary scattering, and accounts for the observation that grain boundaries are less effective than surfaces in scattering electrons. If we proceed to assume that single grains span the film thickness, and the in-plane grain size increases with d to maintain roughly the same axial ratio for the grain (see Sec. III C), then R_g is directly proportional to d. To test this simple model for grain growth, we plot $\tau_{\rm PB}^{-1}$ versus d^{-1} in Fig. 9. Although the linear trend is within the absolute confidence limits due to parameter correlations, our relative confidence appears to be much better. The observed trend with an intercept of $\tau_{{\rm PB},b}^{-1}$ as $d \rightarrow \infty$ is expected from Eq. (3) with λ proportional to d. Thus, we conclude that our hypothesis and assumption concerning boundary scattering and grain growth are valid at least to first order.

As described in Sec. III C below, an analysis of the (ψ,Δ) spectra in the particle growth regime using a generalized Maxwell-Garnett EMT suggests a spheroidal particle shape and axial ratio $\gamma \equiv b/c \sim 2.5$, where b and

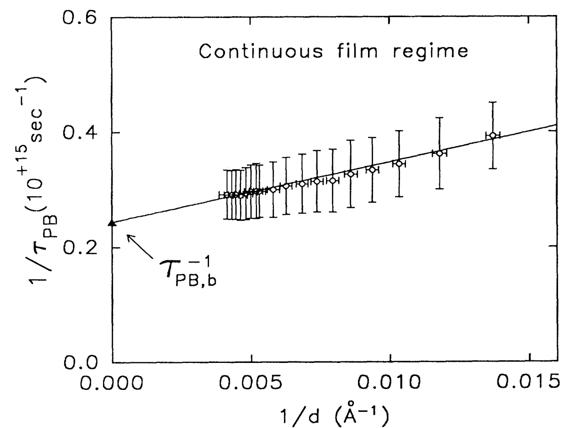

FIG. 9. The parallel-band electron relaxation rate plotted as a function of reciprocal thickness using results in the continuous regime ($d > 60$ Å) for the high-rate Al evaporation of Fig. 8. The solid line is the fit to the data using the relationship of Eq. (3) with λ proportional to thickness. The bulk film relaxation rate, plotted at $d^{-1}=0$, is obtained independently from data collected on the final opaque film. For a grain radius of $d/2$, the slope of the solid line corresponds to a grain-boundary reflection coefficient $\mathcal{R}$ of 0.15. The error bars are the absolute 90% confidence limits in the regression analysis.

c are the semiaxes parallel and perpendicular to the film, respectively. If this shape is retained for the grains in the continuous film growth regime, then the appropriate grain radius for use in the $\lambda \rightarrow \text{func}(R_g)$ substitution falls within the following range:

$$(d/2) < R_g < 2.5(d/2).$$

From this information, along with the Fermi velocity and the slope of the relationship in Fig. 9, the range in the grain-boundary reflection coefficient can be calculated as $0.15 < \mathcal{R} < 0.30$. The lower limit of $\mathcal{R}$, corresponding to $R_g = d/2$, matches an earlier result obtained on Al films from electrical resistivity measurements,[50] and the approximate equality of grain diameter and thickness in Al films has also been noted elsewhere.[51] The fit to λ versus d for the grain growth model is also shown on the semilogarithmic plot of Fig. 8 (solid line).

We conclude this subsection by reiterating the capabilities of real-time spectroscopic ellipsometry for characterization of continuous Al films. The time evolution of the following characteristics can be obtained: (i) the morphology, including thickness and relative grain size; (ii) the optical properties, including both real and imaginary parts of the dielectric function; and (iii) the electronic properties, specifically, the parallel-band electron relaxation time at optical frequencies.

C. Interpretation of the optical functions in the particle growth regime

The particle growth regime will be studied in greater detail for the low-rate Al deposition. The particle nucleation density is lower under these conditions. Thus, isolated particle growth can be observed and the electronic behavior deduced over a wider range of thickness prior to contact. Figure 10 shows the dielectric functions of the particle films determined from (ψ, Δ) by the artifact minimization procedure of Fig. 5, assuming a one-layer, isotropic model for the Al particle film. The dielectric functions are dominated by the resonance absorption band that shifts to the red and increases in magnitude as the particles increase in size, as noted earlier in Sec. III A.

To assess these results and extract information on the electronic behavior, we consider an obviously simplified morphological model of the particle film, consisting of an array of identical substrate-supported spheroids with axes of symmetry perpendicular to the substrate. As will be seen, the consistency of the results of the analysis supports the validity of our approach. With this geometry, we can apply a generalized, anisotropic EMT of the Maxwell-Garnett type:[52,53]

$$\epsilon_{\parallel} - 1 = Q[F_{\parallel} + (\epsilon_i - 1)^{-1}]^{-1}, \quad (4a)$$

$$1 - (\epsilon_{\perp})^{-1} = Q[F_{\perp} + (\epsilon_i - 1)^{-1}]^{-1}. \quad (4b)$$

Here, $\epsilon_{\parallel}$ and $\epsilon_{\perp}$ represent the principal components of the effective dielectric function with $\parallel$ and $\perp$ indicating the directions with respect to the film plane. Q is the Al volume fraction, and ϵ_i is the intrinsic dielectric function of the Al particles. $F_{\parallel}$ and $F_{\perp}$ in Eq. (4) are interaction

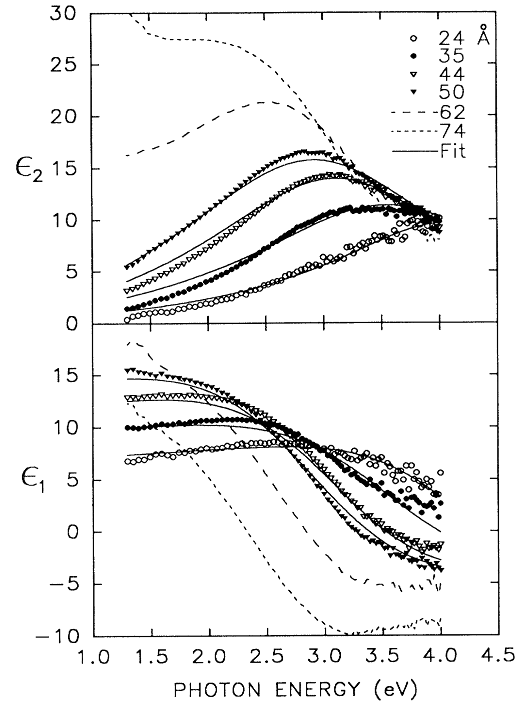

FIG. 10. Selected effective film dielectric functions obtained from real-time observations of low-rate Al evaporation (43 Å/min) determined according to a one-layer, isotropic model using an analysis such as that of Fig. 5. The solid lines are three parameter fits (Al volume fraction Q, electron relaxation time λ, and interaction parameter F_{iso}) using least-squares regression analysis and the generalized EMT of Eq. (4a).

parameters for spheroidal particles, given by

$$F_{\parallel} = f_{\parallel} - \{0.716Qd/[\xi a(\epsilon_s + 1)]\} - \gamma^2(\epsilon_s - 1)/[24(\epsilon_s + 1)], \quad (5a)$$

$$F_{\perp} = f_{\perp} + \{1.432\epsilon_s Qd/[\xi a(\epsilon_s + 1)]\} - \gamma^2(\epsilon_s - 1)/[12(\epsilon_s + 1)]. \quad (5b)$$

ξ is a parameter that depends on the interparticle geometry; ϵ_s is the SiO_2 substrate dielectric function (taken to be constant at 2.17); and $f_{\parallel}$ and $f_{\perp}$ are depolarization factors, which depend only on the axial ratio $\gamma \equiv b/c$ of the particles.[54] Here, b and $c = d/2$ are the semiaxes parallel and perpendicular to the substrate surface. The second and third terms on the right-hand sides represent static dipole interactions among particles and their images in the substrate. The two constant factors in Eqs. (5) (i.e., 0.716 and 1.432) are chosen such that for a square lattice of particles with spacing a, the parameter ξ is 1.0. In this case, the ratio d/a can be eliminated from the second terms in Eqs. (5) using the expression $(d/a) = (6Q/\pi\gamma^2)^{1/2}$, derived from geometrical considerations. For a random distribution of islands, ξ is larger (~ 1.4), and in this case a is interpreted as the average interparticle spacing.[9] On the other hand, for a more closely packed hexagonal lattice, ξ is smaller (~ 0.9).[55]

In the particle growth regime, the Ashcroft-Sturm parametrization for ϵ_i is also used. For the final fits, all parameters are fixed at bulk film values except for the Drude and parallel-band relaxation times which are modified by a common value of λ in accordance with Eq. (3). For selected preliminary fits to (ψ,Δ) spectra, however, we have included the optical mass as a free parameter, but bulk values within the confidence limits are returned in each case. It also turns out that the best-fit values of λ are so small and the parallel-band transition so broadened that the spectra are relatively insensitive to variations in $|U_{200}|$; thus, it is also fixed.

In order to begin the analysis, we assume that the results in Fig. 10 are characteristic of $\epsilon_{\parallel}$.[56] This assumption will be strictly valid only if the film is isotropic. From Eqs. (4), isotropy will occur when

$$\delta_A \equiv |F_{\parallel}-(F_{\perp}-Q)| \sim 0.$$

Thus, we fit the effective film dielectric functions to Eq. (4a) by least-squares regression analysis using three free parameters, Q, $F_{\text{iso}} \equiv F_{\parallel}$, and λ (which defines ϵ_i). The fits are given as the solid lines in Fig. 10. With the best-fit values of $F_{\parallel}$ and Q, Eq. (5a) can be solved for the axial ratio γ. Although different branches to this solution exist, we reject those with $\gamma < 1$ (i.e., prolate spheroids) as being physically unrealistic. Figure 11 shows the oblate branch as a function of thickness for three different choices of the parameter ξ. The two larger values of ξ show reasonable behavior expected for particle growth: a weak flattening of the particles as the film thickness increases. Approximate saturation of this trend to $\gamma \sim 2.5$ is observed for particle thicknesses greater than ~ 40 Å. Lower values of ξ (<1) result in a physically improbable maximum at 40 Å and, thus, can be ruled out.

These results can be compared with an estimate of $\gamma \sim 4$ from *ex situ* transmission electron microscopy (TEM) studies of an Al particle film prepared by high rate evaporation (~ 600 Å/min) onto SiO_2/*c*-Si at room temperature.[57] In this study the mean thickness of the particle film was estimated to be 20 Å, based on the output of a quartz-crystal oscillator. The difference between the values deduced optically and by direct microscopy may arise from a number of factors, including the simplified optical model used for the former result or uncertainties in physical thickness or postoxidation modification for the latter result.

With values for Q, γ, and $F_{\parallel}$, both $F_{\perp}$ and the degree of anisotropy δ_A can be calculated from Eq. (5b). The results for δ_A for different values of the parameter ξ are shown in Fig. 12. We note that for the reasonable range of $1.0 \le \xi \le 1.4$, the anisotropy is very weak ($\delta_A \le 0.05$) for particle films with $d < 40$ Å. This behavior stems from a near cancellation of anisotropies arising from the particle shape and the dipole interaction. Apparently, this holds in the case of Al on SiO_2/Si, but is not a general feature of metal particle films,[58] depending sensitively on the values of Q, γ, and ϵ_s. Figure 12 shows that only the solution to Eqs. (5) with $\xi = 1.0$ (particles on a square grid) provides the satisfying outcome that $\delta_A \rightarrow 0$ as the particles begin to coalesce (solid line). As a result, this solution is adopted here.

With ξ fixed at 1.0, we can now calculate the effective $\epsilon_{\parallel}$ and $\epsilon_{\perp}$ from Eqs. (4) and (5) and then simulate the (ψ,Δ) spectra that would result from Al particle films on SiO_2/Si with such weakly anisotropic dielectric responses. The results are then treated in the same way as the experimental data, i.e., they are subjected to the entire isotropic data analysis procedure, including (i) artifact minimization for determination of the (ϵ_1,ϵ_2) spectra and thicknesses, and (ii) regression analysis of the (ϵ_1,ϵ_2) spectra to deduce $(Q,\lambda,F_{\text{iso}})$. The resulting thicknesses are within 3 Å of the values obtained in the original data analysis, and the latter three free parameter sets are within the confidence limits of the earlier analysis. These results imply self-consistency and that the assumption of isotropy in the original data analysis is valid at least to the desired level of confidence in the de-

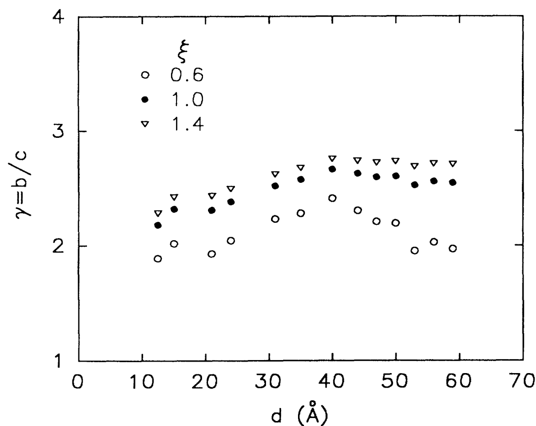

FIG. 11. Spheroidal particle axial ratio as a function of film thickness from Eq. (5a) for different values of the parameter ξ (defined by the distribution of particle nucleation sites). These results were deduced in the particle film regime for low-rate Al evaporation.

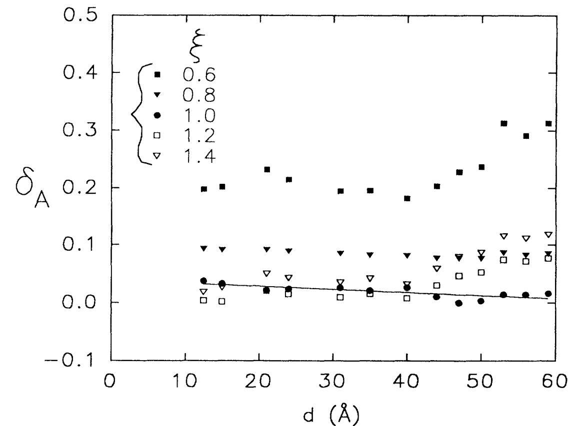

FIG. 12. Degree of anisotropy $|F_{\parallel}-(F_{\perp}-Q)|$ as a function of film thickness from Eqs. (5) for different values of the parameter ξ (defined by the distribution of particle nucleation sites). These results were deduced in the particle regime for low-rate Al evaporation. The solid line is a guide to the eye for the data with $\xi = 1.0$ (particles on a square grid).

duced parameters. In other words, the (ψ,Δ) spectra for an anisotropic film defined by the parameters $(d,Q,\lambda,F_{\parallel},F_{\perp})$ are sufficiently close to the spectra for an isotropic film defined by the set $(d,Q,\lambda,F_{iso}=F_{\parallel})$, such that *a full anisotropic analysis of the data is unnecessary.*

With the validity of the isotropic model now demonstrated, we now discuss the parameters resulting from the fits of Fig. 10. First, the variation in the electron mean free path λ with film thickness in the particle growth regime for the low-rate Al deposition will be discussed. Figure 8 shows λ and τ_{PB}, related through Eq. (3) for the particle growth regime with $d < 60$ Å (circles). Corresponding results for the particle regime for the high-rate Al deposition ($d < 50$ Å) also appear in Fig. 8 (triangles).

First, it is notable that λ (and τ_{PB}) for both low- and high-rate Al depositions in the particle regime connect smoothly to the value(s) for the 53-Å high-rate film above the transition to a continuous structure. The importance of this fact cannot be overemphasized. In the particle regime the generalized Maxwell-Garnett EMT [Eq. (4)] is used in the analysis of the effective dielectric function. Here, λ is determined from the width of the plasmon-polariton absorption band which, as we shall see shortly, is influenced both by the Drude and parallel-band contributions. Above the transition, the Bruggeman EMT is used because the film density is high and particles are no longer present. Here, λ is determined by emphasizing the fit to ϵ_2 at low energies in the region of the (200) parallel-band transition (see Fig. 7). The continuity in λ across the transition implies that the same electronic structure is present even after coalescence of the particles, and the crystallization transition described in Sec. III B is inhibited for a short time (1–2 s or 5–10 Å).

Because of the continuity in λ between the two regimes, we argue that the λ values in the particle regime are, in fact, correct and not erroneously lowered by neglecting particle shape distributions that would also tend to broaden the particle film absorption band (and thereby simulate a reduction in λ). Conversely, we conclude that simplifying the morphological model by neglecting distributions in particle shape and spacing does not compromise the deduced information on the electronic behavior.

Perhaps more interestingly, the values of λ are nearly independent of thickness (8 ± 2 Å) in the particle regime for both depositions. This suggests that the dielectric functions of the particles themselves are dominated, not by scattering at particle surfaces, but rather by scattering events internal to the particles. This provides additional support for an amorphous or nanocrystalline structure for the Al particles. The observation further implies that the effective dielectric function of the film and electronic behavior deduced from Eq. (4a) is relatively insensitive to the Al particle size distribution, i.e., a single Al dielectric function is appropriate for all particles within a given film irrespective of their size. Conversely, we can now conclude that simplifying the morphological model by neglecting distributions in particle size does not compromise the deduced information on the electronic behavior. Further discussion of these points will be presented in Sec. IV.

Finally, in Fig. 13, the particle film effective dielectric function for $d = 50$ Å, along with the fit, are reproduced from Fig. 10. Also included in Fig. 13 is the dielectric function of the particles themselves, decomposed into its Drude and parallel-band parts. We stress that since λ is nearly constant in the particle growth regime, the latter dielectric function is characteristic of the Al particles, irrespective of the thickness of the effective film or its deposition rate. The width of the resonance feature in the effective dielectric function of the film is proportional to the imaginary part of the dielectric function of the particles,[7] which exhibits nearly equal contributions from Drude and parallel-band parts in the neighborhood of the resonance. Thus, the mean free path in the particle regime in Fig. 8 reflects electrons participating in both Drude and parallel-band transitions.

Next, we will discuss the remaining parameters (Q,F_{iso}) deduced in the fits to the effective dielectric functions of Fig. 10. These two parameters are less certain owing to the simplified morphological model that they represent. Figure 14 shows F_{iso} plotted as a function of the Al volume fraction Q for film thicknesses 10 Å $< d <$ 60 Å. The relatively small void volume fraction $(1-Q)$, decreasing from 0.6 to 0.3 as the film thick-

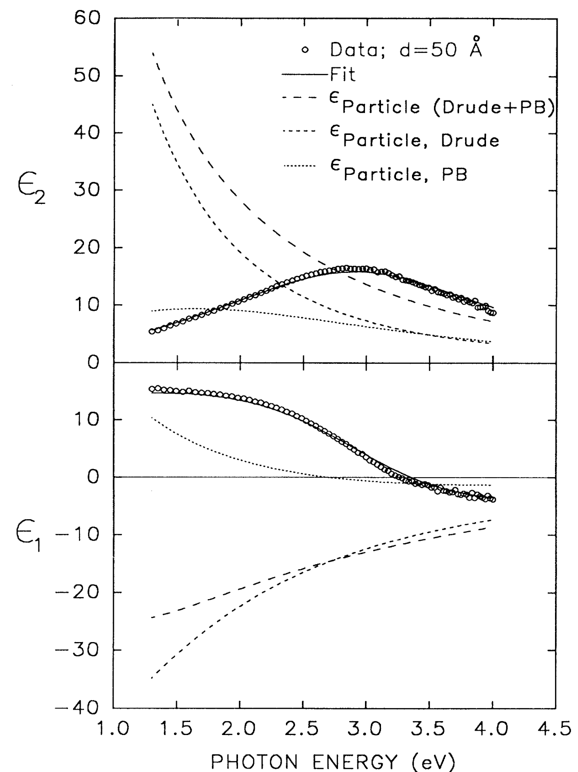

FIG. 13. Effective dielectric function deduced using a one-layer, isotropic model for the 50-Å-thick film prepared by low-rate evaporation (open circles). These results along with the fit (solid line) are reproduced from Fig. 10. Also shown is the dielectric function of the particles themselves determined from the best-fit value of the electron mean free path λ. The particle dielectric function is decomposed into its Drude and parallel-band parts.

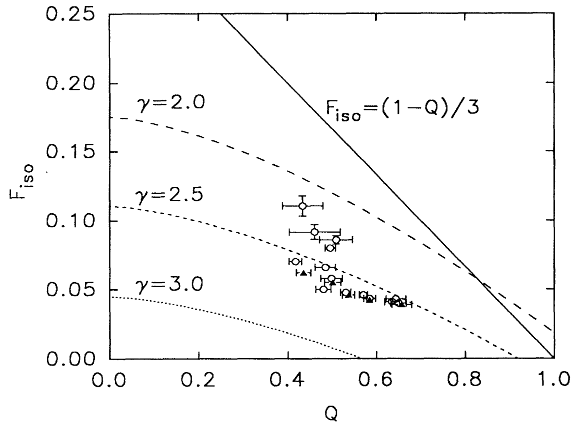

FIG. 14. Interaction parameter $F_{iso}=F_{\|}$ from the generalized Maxwell-Garnett EMT of Eq. (4a) as a function of Al volume fraction obtained in the particle growth regime ($d<50$ Å) for low-rate Al deposition (open circles). The solid triangles are for the film deposited by sputtering. Solid and dashed lines are obtained from the simple Maxwell-Garnett EMT (Ref. 2) and the generalized EMT of Eq. (4a), respectively. The different curves for the latter correspond to different axial ratios (γ) for the assumed spheroidal particles. Error bars are the 90% confidence limits in the regression analysis.

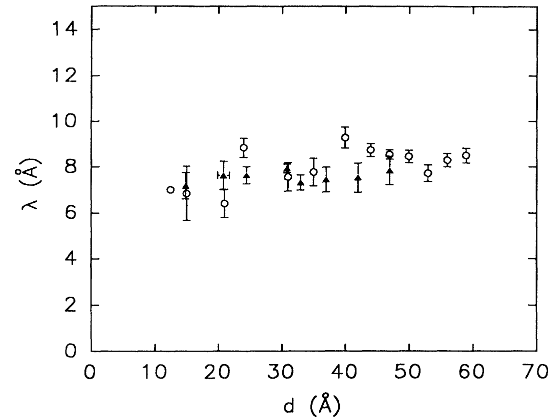

FIG. 15. Electron mean free path as a function of thickness deduced from an analysis of the effective dielectric functions in the particle regime for sputtered (triangles) and low-rate-evaporated (circles) Al films deposited on SiO_2/Si substrates at room temperature. The latter results are reproduced from Fig. 8.

ness increases, is inconsistent with spherical particles that increase in size maintaining the same shape. Instead, the results are consistent with flattened particles that cover a large fraction of the substrate surface. This behavior is reasonable since a closely similar void development has been observed for *a*-Si and *a*-Ge deposition on oxide-covered Si in an analysis employing the Bruggeman EMT.[59] The conclusion that the Al particles are flattened rather than spherical also arises when Eq. (5a) is solved for the axial ratio (see Fig. 11); it is also consistent with the TEM results on Al particle films, as described in Ref. 57.

The broken lines in Fig. 14 show the functional relationship of Eq. (5a) with $\xi=1.0$ for selected values of γ. These curves, when compared with the best-fit values, provide the same information as in Fig. 11. The solid line in Fig. 14 is the expected behavior for spherical particles with the Lorentz field interaction, assumptions that revert Eq. (4a) to the simple EMT originally proposed by Maxwell-Garnett.[60] In contrast to the conclusions of an early study on metal particle films,[10] this simple model is not supported by our results.

We will conclude this section with a comparison of results in the particle growth regime for the low-rate-evaporated Al film (43 Å/min) with those of the magnetron-sputtered Al film having a similar rate (36 Å/min). One-layer, isotropic analyses similar to that of Fig. 5 are performed to deduce (ϵ_1,ϵ_2) from (ψ,Δ) spectra collected in the particle regime during Al sputtering. The results are then interpreted by least-squares regression analysis using Eq. (4a). Figure 15 shows the resulting electron mean free path λ as a function of thickness on an expanded linear scale for the sputtered Al film (triangles). Also included in this figure are the corresponding results for the low-rate-evaporated film, reproduced from Fig. 8 (open circles). For the sputtered film, λ is remarkably constant (within ± 1 Å) for 15 Å $<d<$ 50 Å, and also overlaps the values obtained for the evaporated film. Thus, we conclude that the structure of the particles prepared by sputter deposition is also amorphous or nanocrystalline and similar to that of particles prepared by evaporation. We would expect that if errors were coupled into λ, for example, as a result of the simplified morphological model, λ would be different for evaporated and sputtered films because of the differences in the particle morphology (see the next paragraph). It would be unreasonable to suggest that the errors in the analyses of the films would conspire to generate a morphology-independent λ value. Thus, the results of Fig. 15 also support the validity of the deduced electronic behavior.

Figure 14 also shows the interaction parameter of Eq. (4a) as a function of Al fraction in the film for the sputter deposition (triangles). In general, there is close agreement between the results for sputter deposition and evaporation. The only difference is that for evaporation, in the earliest growth stages ($d\sim$10–15 Å), the particles are closer in shape to spheres. This difference is consistent with the difference in the energetics of the incoming Al. The sputtered species have a higher impact energy, and this tends to generate flatter initial nuclei. For a constant value of λ, the larger value of F_{iso} in the earliest stages of growth for the evaporated particle film in comparison to the sputtered one is manifested in the optical functions as a higher peak energy for the resonance feature in ϵ_2. Thus, as long as the optical functions of the particles themselves do not change, changes in the energy of the maximum in ϵ_2 provide information on changes in particle shape and morphology of the effective film. Increases in the axial ratio, Al volume fraction, and average particle spacing lead to a reduction in F_{iso} [through Eq. (5a)] and a reduction in the energy of the maximum in ϵ_2.

We conclude this section by noting that the overall

time and sample dependences in the deduced morphology conform to our intuition, and this provides some measure of support for their validity. Further confirmation must await direct probes of morphology, but a valid comparison with electron microscopy on this material is expected to be difficult, especially if an accurate axial ratio of the particles is desired. Overall, our results for the optically deduced morphology are in reasonably good agreement with the *ex situ* TEM studies of Roberts and Dobson,[57] given the limitations noted earlier. The growth technique, conditions, and substrate in Ref. 57 correspond rather well to the present one.

IV. DISCUSSION

One of the most important findings of this study is the observation that the electron mean free path λ, as defined by Eq. (3), is nearly independent of Al film thickness and, hence, particle size in the particle growth regime over a relatively wide range, 10 Å $< d <$ 50 Å. This appears to be a general feature of Al particles that nucleate on room-temperature substrates from atomic vapor generated in both evaporation and sputtering processes. In a number of earlier studies of metal particle films, it has been assumed that electron scattering at particle surfaces controls the mean free path. Thus, the relationship of Eq. (3) with λ replaced by a particle dimension (either the particle radius for spheres or the minor semiaxis for spheroids) yields the "classical size effect relationship,"[45,61] which has been a basic ingredient in modeling the optical properties of particle films.[10,11,62] From our work it is clear that such an approach is not valid in general and must be tested for each metal particle system. We will discuss the implications of this work in light of selected results from the literature. In fact, the literature on metal particle optical properties is so extensive, as evidenced by a number of earlier reviews,[43,63–68] that only a representative fraction of the research can be considered here.

To our knowledge, the first clear evidence of the importance of internal defects in metal particles has been made by Kreibig in a study of isolated Ag particles with mean radii from 30 to 200 Å.[69] In this study, the measured resonance absorption band widths were compared with those calculated using a Drude model that incorporates the classical size effect relationship for the particle optical properties. Particles prepared in low-temperature processes ($\leq 100\,°C$) exhibited much larger bandwidths than predicted, whereas those prepared at high temperatures (500–600 °C) exhibited bandwidths in agreement with theory. A conclusion was drawn basically similar to that of Sec. III C, namely, that defects internal to the Ag particles prepared at lower temperatures dominated the electron-scattering processes and led to the disagreement between experiment and theory. However, confidence in this conclusion was tempered by uncertainties in the appropriate size effect relationship for the different preparations. In contrast, the advantage of our real-time approach is clear: The conclusion of internal defect scattering does not rely on the validity of the absolute magnitudes of λ in Fig. 15, but rather the lack of a significant dependence on thickness and, hence, particle size over an estimated factor of 4.

Described earlier in Sec. I, one of the most careful studies of interacting metal particles was performed on Au films prepared by evaporation at 17 °C.[11] This study concentrated on a thickness range similar to that employed for our Al particle films and concluded that the optical properties of discontinuous Au films (and noble-metal films in general) are governed by the morphology of the islands alone. In part, this conclusion was predicated by a critical assumption in the optical analysis, namely, that the size and shape of the particle uniquely defines its dielectric function, as a result of the dominance of electron scattering at the particle surfaces. Specifically, for the distribution of spheroidal particle sizes and/or shapes as quantified by electron microscopy, the mean free path of electrons was equated to the minor semiaxes of the particles. These values were then used to modify the Drude contribution to the dielectric response of the associated particles, retaining bulk film values for the interband contribution. As a result of this analysis approach, a single free parameter was used in fitting the normal incidence transmittance spectra of the Au particles—basically, the geometric parameter ξ of Eqs. (5) which quantifies the distribution of interparticle separations.

Although the fits in Ref. 11 were deemed satisfactory, significant discrepancies were obtained, particularly in the width of the minimum in the transmittance spectra of the films with mass thicknesses between 25 and 40 Å. In fact, discrepancies of up to 25% in the transmittance were observed for the thickest films as a result of a significantly broader bandwidth in the transmittance minimum for the data in comparison with the fit. This was attributed to irregular islands for the thicker films whose optical properties could not be established with confidence. It is also possible that the discrepancies arise as a result of an inappropriate application of the classical size effect relationship.

Our goal here is not to reinterpret the earlier results, but to gain additional insights into this problem by further inspection of representative Al particle film optical functions. Figure 16 shows the effective dielectric function (points) of the 50-Å-thick film of Figs. 10 and 13, along with the three-parameter best fit (solid line) that provides $Q = 0.58$, $F_{iso} = 0.044$, and $\lambda = 8.5$ Å. To obtain the dashed line, we fixed $\lambda = d/2 = 25$ Å, a minimum value to be expected within the validity of the classical size effect relationship [Eq. (3) with $\lambda \sim$ minor semiaxis]. The values of F_{iso} and Q were then chosen to match the peak height and position of the absorption band in ϵ_2, as is often done in matching transmittance minima in earlier studies. For the dotted line in Fig. 16, the electron relaxation times for bulk film Al were used [i.e., Eq. (3) with $\lambda \to \infty$]. The results for $\lambda = 25$ Å demonstrate clearly the magnitude of the problem that arises in associating λ with a particle dimension in the case of Al.

In Fig. 17 we present "experimental" transmittance spectra as a function of photon energy generated from the Al dielectric functions from Fig. 10 for the low rate evaporation. For simplicity the transmittance was calcu-

lated assuming a free-standing film, as would be expected for a measurement that properly accounts for the substrate. For comparison with typical literature results, the solid lines represent fits to the experimental dielectric function, converted to transmittance spectra in the same manner. It should be kept in mind, however, that these fits match not only the transmittance but also adequately reproduce the full complex optical response. We find agreement between the "experimental" and fitted results to within $\sim 2\%$ in the transmittance.

This agreement represents a significant improvement over earlier such attempts for metal particle systems. If we were to fix the mean free path at 8 ± 2 Å for the full series of spectra, the fits of Fig. 17 can be achieved in the absence of any other characterization by varying only two morphological parameters, Q and $F_{\parallel}$. We conclude that although there is a clear role of the particle shapes and spacings in establishing the optical properties, equally significant information is present on the defects in the particles themselves. Thus, real-time SE provides not only important information on morphology and optical properties of particle films but also information on the crystalline perfection of the particles.

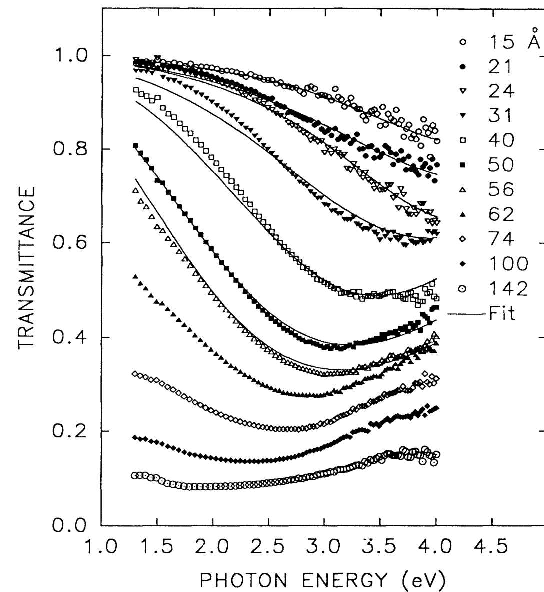

FIG. 17. Evolution of the transmittance spectra with thickness for the low-rate Al evaporation (symbols) calculated from the experimental dielectric functions of Fig. 10 assuming a free-standing film. The solid lines correspond to the models such as those in Fig. 10 that provide the best fits to the dielectric functions.

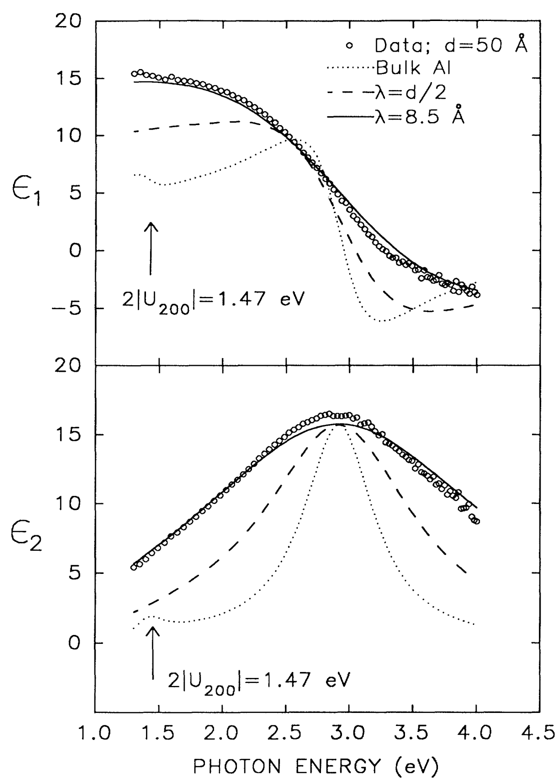

FIG. 16. Effective dielectric function for the 50-Å-thick Al film (circles) prepared by low-rate evaporation along with the best three-parameter fit (solid line), both reproduced from Fig. 10. The electron mean free path λ for the best fit is 8.5 ± 0.3 Å. For the dashed-line result, λ is fixed at $d/2=25$ Å, and $F_{\rm iso}$ and Q are chosen to match the absorption peak position and amplitude (0.037 and 0.28, respectively). For the dotted-line result, the bulk film dielectric function for the Al particles is chosen, and $F_{\rm iso}$ and Q are fixed at 0.035 and 0.13. The arrow denotes the position of the (200) parallel-band feature, visible in the latter spectra.

One of the most advanced previous studies of the optical properties of Al particles was reported in Ref. 62 on thick Al soot deposits prepared by gas evaporation in He/O_2. The overall approach was similar to the study of Ref. 11 in that attempts were made to predict the transmittance spectra of the deposits solely from the morphology provided by electron microscopy. In this case, however, the morphology was much less certain because of the experimental difficulties. One free parameter, associated with the thickness of the dielectric coating on the particles, was needed in the fits. As in the case of the Au films, the Drude contribution to the dielectric response was modified by the classical size effect relationship, [i.e., Eq. (3) with λ proportional to particle size], but the interband contribution was fixed at the bulk film response. The parallel-band transition in Al, which is quite sharp in the bulk films, as seen in Fig. 3, permitted a more realistic assessment of the suitability of the fit, in comparison to that for Au particle films. It was found that the parallel-band feature in the modeled transmittance was well defined, in poor agreement with the smeared-out feature in the experimental spectra.

The overall fit to the data in Ref. 62 was somewhat improved by using a mean free path for the Drude contribution of 5 Å, which is much shorter than the average metal particle radius (~ 15 Å), but close to the values obtained in our study (8 ± 2 Å). This result suggests that the gas-evaporated particles exhibit a defective internal structure similar to that of the particles studied here. In spite of this improvement, the fits to the transmittance

spectra still deviated significantly (by 9–12% in transmittance) in the neighborhood of the parallel-band feature. Our results suggest that the origin of this problem lies in the use of the bulk film relaxation time for the parallel-band contribution. In the computed dielectric functions of Fig. 16, a feature at the parallel-band energy of 1.47 eV is observed only for the case in which a bulk relaxation time is assumed; otherwise, the feature is broadened beyond recognition (see Fig. 13). Finally, we note that one study has suggested that the complete absence of a parallel-band feature in the transmittance spectra of gas-evaporated particles can be attributed to quantum size effects,[70] applying the theoretical work of Wood and Ashcroft.[71] However, in our transmittance spectra in Fig. 17, the feature is similarly absent and the results can be fit quite closely with a simple mean-free-path effect on *both* Drude and parallel-band contributions. The fit is in fact close enough to the experimental results that it is difficult to take the analysis further to include quantum size effects.

Our determination of the λ values differs from previous studies of metal particles for three reasons. First, both real and imaginary parts of the optical functions were deduced from our measurements and fitted by the optical model, whereas many previous studies have usually employed transmittance and/or reflectance measurements to determine only ϵ_2 (or α, the absorption coefficient). Second, our optical model includes the effects of variable λ on both Drude and parallel-band contributions. Third, our measurements are performed *in situ* during preparation, and therefore additional parameters associated with oxidation or other atmospheric contamination effects (which must be included even with direct morphological analysis by electron microscopy) are avoided.

Next we will discuss in further detail the atomic structure of the evaporated Al film for thicknesses less than the mean-free-path transition in Fig. 8, but above the apparent percolation threshold (defined by the onset of metallic behavior in ϵ_1). The shape of the effective dielectric response of the film is not as strongly influenced by the morphology in this regime in comparison to the particle growth regime where Eqs. (4) are used. Figure 18 shows the imaginary part of the dielectric function for the 53-Å film prepared by high-rate Al evaporation (points). (The corresponding real part appears in Fig. 6.) In order to fit this dielectric function, we must set $\lambda \sim 10 \pm 1$ Å, giving both Drude and parallel-band relaxation times of $\sim 4 \times 10^{-16}$ s. In Fig. 18 we compare these results to those for other pure Al systems in which the parallel-band absorption is also found to be absent: (i) liquid Al at 900 °C (Ref. 46) and (ii) evaporated Al quenched in thin-film form onto a substrate at 25 K.[72]

There are significant differences among the dielectric functions for the different materials even though they are all pure Al. The liquid Al shows behavior in ϵ_2 that can reasonably be accounted for with a single Drude term with an electron relaxation time of 9.7×10^{-16} s ($\lambda = 22$ Å).[46] In contrast, initial studies suggested that both Drude and interband components are required to fit the data for quenched samples.[72] The former can be fit with a relaxation time of 3.4×10^{-15} s ($\lambda = 100$ Å), and

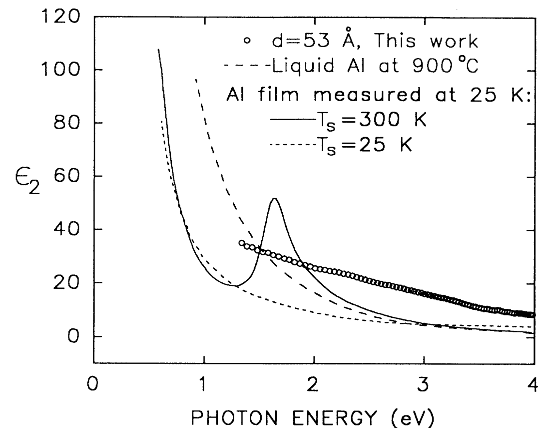

FIG. 18. Imaginary parts of the dielectric function for different Al materials: 53-Å-thick Al obtained by high-rate evaporation in the continuous film growth regime (open circles), opaque Al film evaporated onto substrates held at 25 K and measured at 25 K (dotted line, after Ref. 72), and liquid Al at 900 °C (dashed line, after Ref. 46). The result is also presented for an Al film evaporated onto a room-temperature substrate and measured at 25 K (solid line, after Ref. 72).

the latter showed characteristics of the (111) parallel-band transition. A subsequent analysis of the dielectric response of the quenched film, however, suggested that it consisted of a two-phase morphology with roughly a third of the material in the form of nanocrystalline grains and the remainder in a disordered intergranular phase.[73] The relaxation times for electrons in the two phases differ by an order of magnitude, 1.8×10^{-16} s ($\lambda = 4$ Å) and 2.2×10^{-15} s ($\lambda = 55$ Å), respectively, with the latter value consistent with the grain size deduced in electron-diffraction studies. In a study of a number of nanocrystalline metals, Hunderi and co-workers have concluded that the electron relaxation time in the intergranular material is shorter than it is in the corresponding liquid and amorphous-metal phases.[73] In fact, when the true amorphous-metal phase can be prepared, its optical spectra in general can be fit with a single Drude contribution.

In view of such considerations, it is reasonable to rule out both single-phase liquid and amorphous thin-film structures to account for the ϵ_2 spectrum of the 53-Å-thick film because its shape is inconsistent with a single Drude contribution. It is tempting, on the other hand, to suggest that the optical response is generated by a dominant intergranular phase in a nanocrystalline composite in analogy with the results for the quenched films. Unfortunately, the two-phase analysis of Ref. 73 has completely neglected the interband components for both phases. For example, when $\lambda = 55$ Å, the (200) parallel-band contribution to ϵ_2 dominates the Drude contribution by a factor of 2–4 over the 1.5–4.0-eV range. As a result, we must question the validity of the numerical results of Ref. 73. At this point, we conclude that the Al structure just prior to the formation of larger crystals (with size approximately equal to thickness) is unlike that of thick quenched Al, which is typically nanocrystalline (50-Å grains).[74] It is possible that the particles are com-

posed of even smaller nanocrystalline grains, or are in fact single crystals, but with a very high density of defects. Such conclusions are supported by the transmission-electron-diffraction study of Ref. 57 in which Al particle films prepared by evaporation onto SiO_2/c-Si to a mean thickness of 20 Å exhibit broadened rings that suggest aggregates of randomly oriented nanocrystals.

Finally, we might consider for a moment the possibility that the 53-Å Al film is two-phase in another respect: one phase consisting of continuous film volume and another phase of isolated particle volume. This type of two-phase morphology does appear to account for the complicated dielectric response of low-rate films which exhibit a low nucleation density, a wider statistical distribution in the particle spacing, and hence more gradual coalescence behavior. For example, for the 74-Å low-rate film of Fig. 10, the shoulder near 2.0 eV superimposed on the falling Drude contribution of the ϵ_2 spectrum suggests such a morphology. However, the broadened dielectric function of the 53-Å film can be fit assuming that the same low mean free path applies to both the parallel-band and Drude contributions (see Fig. 13 for separate contributions). In summary, we suspect that the structure at this particular stage of the growth dynamics is far from equilibrium, but further information must await kinetic analysis by high-speed real-time structural probes.

V. SUMMARY

We have determined the optical functions of thin metal films throughout the nucleation and growth stages using a multichannel ellipsometer. Parallel detection over the photon-energy range from 1.3 to 4.0 eV provided acquisition times as short as 0.3 s for the ellipsometric spectra, allowing real-time measurement with monolayer resolution and sensitivity at film growth rates up to 280 Å/min. Our study was performed on aluminum films prepared both by evaporation and sputtering onto thermally oxidized Si substrates, in part because of the technological importance of characterizing the relationship between Al morphology and optical properties for various applications. More importantly still, the theoretical framework has been developed that relates the optical properties of Al to its electronic band structure, and extensive experimental studies have validated the framework. The prior developments allow us to express the dielectric function of Al in terms of a few photon-energy-independent parameters so that the evolution of electronic characteristics can be studied in the nucleation and growth stages. We include the effects of electron scattering by surfaces, subsurface defects, and grain boundaries, in modifying both the Drude and interband contributions to the dielectric function of Al particles and bulklike films. We believe this is the key to an overall improved agreement between experiment and theory which characterizes this study in comparison to earlier ones. For a detailed analysis of the particle growth regime, we concentrated on films prepared by evaporation and sputtering at relatively low rates ($\sim$40 Å/min). For the continuous film growth regime, an evaporated film deposited at a factor-of-7-higher rate was studied.

In the particle regime of growth for low-rate Al evaporation (typically for thicknesses $d < 60$ Å), the dielectric functions have been extracted using a one-layer, isotropic optical model. A very good fit to the dielectric functions has been obtained using a generalized Maxwell-Garnett effective medium theory and a simplified morphological model. The EMT includes dipole interactions between identical spheroidal particles and their images in the substrate. In general, the fit involves three free parameters: the electron mean free path (λ), which characterizes the particle optical functions; the Al volume fraction (Q); and an interparticle interaction parameter (F) which depends on particle shape, average spacing, and Q. We have found that for acceptable solutions for the particle shape, the predicted particle film anisotropy inherent in the generalized EMT is negligible owing to a near cancellation of anisotropies associated with the particle shape and dipole interaction. This provided the necessary justification of the isotropic model used to extract the effective dielectric functions of the film. The deduced evolution of the interparticle interaction and the Al volume fraction ruled out the classical Maxwell-Garnett EMT with the Lorentz field interaction for the growing particles. Support for the morphological model comes in part from the fact that the evolution of Q with thickness is very similar to that observed in other thin-film systems we have studied and suggests flattened particles covering a large fraction of the substrate surface.

For all Al particle films studied by evaporation at different rates and by sputtering, the electron mean free path λ for 10 Å $< d <$ 50 Å is nearly constant in the range of 8 ± 2 Å. The simplifications employed in the morphological model (i.e., neglect of the statistical distributions in particle size, shape, and spacing) do not appear to lead to errors in the deduced λ values. Near the resonance peak associated with dipolar plasmon-polariton excitations in $\sim$50-Å particles, the imaginary parts of the dielectric functions of the particles themselves are influenced equally by the Drude and parallel-band contributions for $\lambda = 8$ Å. This fact demonstrates the importance of including modifications to the electron relaxation time for both contributions.

Because the mean free path is independent of particle film thickness and, hence, particle size, electron scattering at defects within the particles rather than at their surface controls the optical response of the particles. Thus, the widely used classical size effect relationship, in which the mean free path is set equal to a particle dimension, is not a valid assumption in general, and its validity must be demonstrated on each system prior to application. We suggest that transmittance spectra of Au particle films and gas-evaporated Al deposits studied earlier may also be influenced by defects internal to the particles. Finally, we conclude that, owing to the possibility of defect scattering within particles, it is impossible to predict the optical response of metal particle films solely from electron-microscopy-based morphological quantification. The exact nature of the particle structure that leads to a

high density of electron-scattering centers is not clear at present. It is likely that each particle is composed of a few connected nanocrystalline subunits with a defective intergranular phase.

For high-rate-evaporated Al, the percolation threshold is found to occur near a film thickness of 45–50 Å. Even across this threshold, the electron mean free path remains low, suggesting that the continuous film still has a highly defective structure, as indicated by the complete absence of the (200) parallel-band feature in ϵ. It is possible that the film remains in a nonequilibrium, nanocrystalline state during the coalescence process. Although there is evidence of a two-phase structure consisting of particle-like and continuous-film-like dielectric responses in the lower-rate depositions, this does not appear to occur for the high-rate Al, and the transition between a particle structure and continuous film structure is abrupt.

Shortly after continuous film formation for the high-rate-evaporated Al, there is a similarly abrupt transition whereby the electron mean free path increases by nearly an order of magnitude (from 10 to 90 Å) over the thickness range of 55–60 Å. This may represent a transition in the continuous film from a nanocrystalline structure to one in which single-crystalline grains span the thickness of the film. Only after this transition is a well-defined (200) parallel-band transition observed. For thicknesses $d > 60$ Å, the mean free path increases with film thickness, as would be expected if electron scattering at grain boundaries dominates the continuous film dielectric function.

ACKNOWLEDGMENTS

Primary funding for this research from the National Science Foundation, under Grant No. DMR-8957159, as well as from Philips-DuPont Optical Company and the DuPont Corporation, is gratefully acknowledged. One of us (I.A.) was also supported by the NSF under Grant No. DMR-8901031.

[1]M. Faraday, Philos. Trans. R. Soc. London **147**, 145 (1857).
[2]J. C. Maxwell-Garnett, Philos. Trans. R. Soc. London, Ser. A **203**, 385 (1904); **205**, 237 (1905).
[3]R. S. Sennett and A. D. Scott, J. Opt. Soc. Am. **40**, 203 (1950).
[4]E. David, Z. Phys. **114**, 389 (1939).
[5]H. Schopper, Z. Phys. **130**, 565 (1951).
[6]S. Yamaguchi, J. Phys. Soc. Jpn. **15**, 1577 (1960); **17**, 184 (1962).
[7]A. Meessen, J. Phys. (Paris) **33**, 371 (1972).
[8]T. Yamaguchi, S. Yoshida, and A. Kinbara, J. Opt. Soc. Am. **64**, 1563 (1974).
[9]D. Bedeaux and J. Vlieger, Physica (Utrecht) **73**, 287 (1974).
[10]R. H. Doremus, J. Appl. Phys. **37**, 2775 (1966).
[11]S. Norrman, T. Andersson, C. G. Granqvist, and O. Hunderi, Phys. Rev. B **18**, 674 (1978).
[12]T. Andersson and C. G. Granqvist, J. Appl. Phys. **48**, 1673 (1977).
[13]Y. Yagil and G. Deutscher, Thin Solid Films **152**, 465 (1987).
[14]P. Gadenne, A. Beghdadi, and J. Lafait, Opt. Commun. **65**, 17 (1988).
[15]M. Kunz, G. A. Niklasson, and C. G. Grandqvist, J. Appl. Phys. **64**, 3740 (1988).
[16]Y. Yagil and G. Deutscher, Appl. Phys. Lett. **52**, 373 (1988).
[17]D. E. Aspnes, E. Kinsbron, and D. D. Bacon, Phys. Rev. B **21**, 3290 (1980).
[18]D. E. Aspnes, Proc. Soc. Photo-Opt. Instrum. Eng. **276**, 188 (1981).
[19]D. A. G. Bruggeman, Ann. Phys. (Leipzig) **24**, 636 (1935).
[20]D. E. Aspnes and H. G. Craighead, Appl. Opt. **25**, 1299 (1986).
[21]B. T. Sullivan and R. R. Parsons, J. Vac. Sci. Technol. A **5**, 3399 (1987).
[22]N. W. Ashcroft and K. Sturm, Phys. Rev. B **3**, 1898 (1971).
[23]H. Ehrenreich, H. R. Philipp, and B. Segall, Phys. Rev. **132**, 1918 (1963).
[24]N. W. Ashcroft, Philos. Mag. **8**, 2055 (1963).
[25]H. V. Nguyen, I. An, and R. W. Collins, Phys. Rev. Lett. **68**, 994 (1992).
[26]J. H. Halford, F. K. Chin, and J. E. Norman, J. Opt. Soc. Am. **63**, 786 (1973).
[27]D. E. Aspnes and A. A. Studna, Phys. Rev. B **27**, 985 (1983).
[28]I. H. Malitson, J. Opt. Soc. Am. **55**, 1205 (1965).
[29]C. A. Neugebauer, in *Handbook of Thin Film Technology*, edited by L. I. Maissel and R. Glang (McGraw-Hill, New York, 1970), Chap. 8.
[30]J. R. Black, IEEE Reliability Phys. Conf. **15**, 257 (1977); R. J. Blattner and A. J. Braundmeier, J. Vac. Sci. Technol. **20**, 320 (1982).
[31]Y.-T. Kim, R. W. Collins, and K. Vedam, Surf. Sci. **233**, 341 (1990).
[32]G. Laurence, F. Hottier, and J. Hallais, Rev. Phys. Appl. (Paris) **16**, 579 (1981).
[33]N. V. Nguyen, B. S. Pudliner, I. An, and R. W. Collins, J. Opt. Soc. Am. A **8**, 919 (1991).
[34]R. M. A. Azzam and N. M. Bashara, *Ellipsometry and Polarized Light* (North-Holland, Amsterdam, 1977).
[35]I. An and R. W. Collins, Rev. Sci. Instrum. **62**, 1904 (1991).
[36]EG&G Princeton Applied Research Corp., Princeton, NJ 08543; OMA III Detector Interface Model No. 1461.
[37]E. Shiles, T. Sasaki, M. Inokuti, and D. Y. Smith, Phys. Rev. B **22**, 1612 (1980).
[38]D. Y. Smith, E. Shiles, and M. Inokuti, in *Handbook of Optical Constants of Solids*, edited by E. D. Palik, (Academic, Orlando, 1985), p. 369.
[39]A. G. Mathewson and H. P. Myers, Phys. Scr. **4**, 291 (1971); J. Phys. F **2**, 403 (1972).
[40]D. E. Aspnes, J. B. Theeten, and F. Hottier, Phys. Rev. B **20**, 3292 (1979).
[41]I. An, H. V. Nguyen, N. V. Nguyen, and R. W. Collins, Phys. Rev. Lett. **65**, 2274 (1990).
[42]H. Arwin and D. E. Aspnes, Thin Solid Films **113**, 101 (1984).
[43]See, for example, U. Kreibig and L. Genzel, Surf. Sci. **156**, 678 (1985).
[44]S. Kar, R. Varghese, and S. Bhattarcharya, J. Vac. Sci. Technol. A **1**, 1420 (1983).
[45]J. Euler, Z. Phys. **137**, 318 (1954).

[46]J. C. Miller, Philos. Mag. **20**, 1115 (1969).
[47]M. Takagi, J. Phys. Soc. Jpn. **9**, 359 (1954).
[48]P. Buffat and J.-P. Borel, Phys. Rev. A **13**, 2287 (1976).
[49]G. A. Niklasson, D. E. Aspnes, and H. G. Craighead, Phys. Rev. B **33**, 5363 (1986).
[50]A. F. Mayadas and M. Shatzkes, Phys. Rev. B **1**, 1382 (1970).
[51]R. Meservey and P. M. Tedrow, J. Appl. Phys. **42**, 51 (1971).
[52]T. Yamaguchi, S. Yoshida, and A. Kinbara, Thin Solid Films **21**, 173 (1974).
[53]T. Yamaguchi, H. Takahashi, and A. Sudoh, J. Opt. Soc. Am. **68**, 1039 (1978).
[54]J. A. Osborn, Phys. Rev. **67**, 351 (1945); E. C. Stoner, Philos. Mag. **36**, 803 (1945).
[55]E. C. Chan and J. P. Marton, J. Appl. Phys. **45**, 5004 (1974).
[56]A previous study suggests that this is the appropriate choice that leads to the correct result; see M. L. Jones, H. H. Soonpaa, and B. S. Rao, J. Opt. Soc. Am. **64**, 1591 (1974).
[57]S. Roberts and P. J. Dobson, Thin Solid Films **135**, 137 (1986).
[58]T. Yamaguchi, S. Yoshida, and A. Kinbara, J. Opt. Soc. Am. **62**, 634 (1972).
[59]R. W. Collins, I. An, H. V. Nguyen, and T. Gu, Thin Solid Films **206**, 374 (1991).
[60]D. N. Jarrett and L. Ward, J. Phys. D **9**, 1515 (1976).
[61]C. v. Fragstein and H. Roemer, Z. Phys. **151**, 54 (1958).
[62]C. G. Grandqvist and O. Hunderi, J. Appl. Phys. **51**, 1751 (1980).
[63]O. S. Heavens, *Optical Properties of Thin Solid Films* (Dover, New York, 1954).
[64]P. Rouard and P. Bousquet, Prog. Opt. **4**, 145 (1965).
[65]L. Genzel, Festkoerperprobleme **14**, 183 (1974).
[66]P. Rouard and A. Meessen, Prog. Opt. **15**, 79 (1977).
[67]G. C. Papavassiliou, Prog. Solid State Chem. **12**, 185 (1979).
[68]J. A. A. J. Perenboom, P. Wyder, and F. Meier, Phys. Rep. **78**, 173 (1981).
[69]U. Kreibig, Z. Phys. B **31**, 39 (1978).
[70]V. V. Truong, P. Courteau, and J. Singh, J. Appl. Phys. **62**, 4863 (1987).
[71]D. M. Wood and N. W. Ashcroft, Phys. Rev. B **25**, 6255 (1982).
[72]L. G. Bernland, O. Hunderi, and H. P. Myers, Phys. Rev. Lett. **31**, 363 (1973).
[73]O. Hunderi, Thin Solid Films **37**, 275 (1976).
[74]W. Buckel, Z. Phys. **138**, 136 (1954); H. Bulow and W. Buckel, *ibid.* **145**, 141 (1956).